Romain JAN
romain.jan@isae-supaero.fr

Experimental validation of ASWING. Part II: Propellers

Supervisors:
- Prof J-M. Moschetta
- Prof J-P. Condomines

ISAE-Supaero: Technical report, ISAE-ASW-2 2024

Abstract

This technical report is the second part of an experimental evaluation and modification of an aeroelastic framework (ASWING). In this chapter, the propeller model is investigated. First, the theoretical models are briefly presented by referring to the fundamental work in the literature on which ASWING is based. The second part of the paper is dedicated to the experimental validation of the model. The ASWING predictions of propeller thrust and efficiency are evaluated against several propellers from the modern literature. In the light of the results, a modification of the model is proposed to increase its accuracy. Secondly, the non-axial flow condition is presented where the normal force, yaw moment and thrust predictions are investigated. Thirdly, experimental data are used to evaluate the jet and swirl velocity field prediction in static and advanced flow conditions. Finally, the ability of ASWING to predict the interactions and their consequences between a propeller jet and a lifting surface is presented. With the exception of the normal and yaw moment predictions, ASWING shows good agreement with the experimental data.

Important note to the reader:
This work has not been peer reviewed yet. Only the author's PhD referee members (Professors Mark Drela, Rafael Palacios, Eric Laurendeau and Murat Bronz) had access to this work and have authorised the defence.For more details, please refers to https://www.theses.fr/s251420. Nevertheless, this material is in a process of publication in peer reviewed journals, in a shorter version. This document will be updated if new material has to be added.

About the data presented in this report:
This report presents various comparisons with different sets of experimental data. The latter and numerical simulations are available on demand. However, if you consider using them for your own studies, please cite this work and the related ones from which data are coming. Contact: romain.jan@isae-supaero.fr

Version notes

This technical report aims to be updated if new experimental cases and ASWING modifications have to be added. Also, the updates aim to take into account the feedback of the community (typos, theoretical development mistakes, etc).
Versioning syntax:
The version of this document is given as follows: II.X.y, where I denotes the second part of this experimental evaluation, X and y denote respectively major and minor updates.

- ***Version II.1.0:***
  (30/07/2023) This version is the one submitted to the author's PhD referee as a partial fulfilment of the PhD degree. This version presented the following experimental cases:
  - CASE A - Propeller thrust and torque predictions. Two propellers in static and advanced flow conditions.
  - CASE B - Thrust, normal force and yaw moment due to an axial flow. One propeller has been used
  - CASE C - Propeller slipstream measurements. Two propellers in static and advanced flow conditions have been used.
  - CASE D - Propeller slipstream/lifting surface. interaction. Two cases were used. One for the effect of the propeller on the lift distribution. Another for the effect of the lateral and vertical position of the propeller and the lift-to-drag ratio.
- ***Version II.1.1:***
  (16/01/2024) Major typos have been corrected.
- ***Version II.1.2:***
  (7/05/2024) Cases have been renamed to $\mathcal{P}$-1 to 5 an $\mathcal{AP}$-1 and 2 to match the formalism used in the other reports for publication purposes. A table has been added to list them and their purposes.

Contents

1 Introduction **6**

2 Theoretical model **6**

2.1 Summary 6

2.2 P-factor model for whirl flutter analysis: 8

3 Experimental validation **12**

3.1 CASES P 1 and 2 - Propeller thrust and torque predictions 12

3.2 CASE P-3 Thrust, normal force and yaw moment due to a axial flow 14

3.3 CASE P 4 and 5 Propeller slipstream measurements 17

3.4 CASE AP-1 Propeller slipstream/lifting surface interaction 19

4 Conclusions: **23**

5 Appendix - A : Complementary data, and propellers geometries **23**

References **28**

1 Introduction

With the rise of computer power over the past 50 years, more sophisticated propeller modelling techniques are used against the historical Froude's momentum theory (Actuator disk theory). From unsteady/steady vortex lattice/vortons methods (UVLM/UVPM) to large eddy simulation (LES), they can provide very sophisticated insights into fluid mechanisms. For example, recently they allowed the acoustic and aerodynamic optimization of turbo propellers and Unmanned Aerial Vehicles (UAV) Li Volsi et al. (2022). Moreover LES and URANS provided more insight into the effect of rugosity on UAV propeller efficiency. However, when it comes to flight mechanics, such a high level of accuracy is not necessary to provide reasonable results and insights. Thus the extended actuator disk theory (EADT) is still used in modern applications to provide first-order insight into different types of applications. When the EADT is coupled to a wake and P-factor model, the field of application becomes wider. The latest version of ASWING (5.96) provides such a model (Drela, 1999, 2008 and 2009). Thus this report is the second part of an evaluation sequel work of ASWING. This paper is only dedicated to the propeller model. The first part of this report aims to provide a historical review of the theoretical model based on literature by recalling the milestone papers that led to the current model. Also, the conservative assumptions made by the author will be highlighted and discussed when needed. In the second part of this paper, an experimental evaluation of the model is presented. In particular a comparison between the static and dynamic thrust prediction and experiments using (Deters et al. 2014a, 2014 and 2014b)'s works. The effects of blade number, advance ratio λ, and Reynolds number R_e (or rotation rate Ω) are investigated. Then the P-factor model is evaluated against Leng et al. 2019, 2020 data. Normal force, yaw moments, and thrust due to non-axial flow are compared to the Leng et al.'s non-linear model. This case is mainly chosen to draw the boundary limits of the P-factor model. Then, the jets axial and swirl velocity predictions of 3 different propellers in static and dynamic conditions are presented against Deters et al. Deters's experiments (2014 and 2015). Velocities are evaluated at different radial and streamwise positions. In light of the results, a new jet model taking into account the effect of the propeller hub is presented and compared. Finally, the capacity of ASWING to predict the interaction between a propeller jet and a lifting surface is investigated. In particular, the effect on the wing lift distribution at several angles of attack and rotation directions. Also, the effect of the vertical and spanwise position of a propeller on a downstream wing lift/drag ratio is presented. The latter cases are studied using the data of Veldhuis 1996, 2004, and 2005.

2 Theoretical model

2.1 Summary

Extended Actuator Disk Theory:
The ASWING extended actuator disk model is used to compute the steady aerodynamic thrust and torque of a propeller. Two main extensions to the initial Rankine-Froude Rankine (1865) and Froude (1889) airscrew theory are implemented. First of all, viscous losses can be considered with an approximation of the power losses due to drag through a constant term as follows

$$\mathcal{P}_v \sim \frac{1}{2}\rho\left(V_e^2+\Omega_e^2R_e^2\right)^{1/2}\left(V_e^2+3\Omega_e^2R_e^2\right)(C_DA)_e \tag{1}$$

where V_e is the upcoming freestream velocity or air-relative speed at the engine shaft. Ω_e, R_e and $(C_DA)_e$ are respectively the engine rotation rate, radius and total effective blade area. Those last 3 parameters are user-defined. Note that $(C_DA)_e$ is reported by the author (Drela 2009) to vary only with the propeller blade number B as

$$(C_DA)_e = BR_ec(0.8R_e)c_d(0.8R_e) \tag{2}$$

Thus a single set $(c(0.8R_e),\ c_d(0.8R_e))$ can define different propellers having 2, 3, 4 etc blades. This feature is discussed in the evaluation section. Equation 1 brings conservatism as it gives an approximation of the viscous loss and not the exact solution to the blade element theory drag integrand. Moreover, $(C_DA)_e$ is assumed not to vary with neither the blade local Reynolds number (or rotation rate Ω) nor the advance ratio λ. Those approximations are discussed in the evaluation section. The axial momentum theory is then extended by taking into account the swirl losses due to propeller tip vorticity. This extension was early presented after Froude-Rankine by Betz Betz (1920) based on the assumption of angular momentum constancy along the propeller blade. However, in ASWING the swirl losses are approximated by an "empirical" term as follows:

$$\mathcal{P}_{sw} = \frac{1}{2}5\lambda^2\Delta V_eF_e \tag{3}$$

with F_e the engine thrust, λ the advance ratio and ΔV_e the flow increment speed at the propeller position. We have not found yet this formulation in the literature except in the author's work (Drela 2009). Glauert(*chapter 1*) presented the general momentum theory where a similar simplification is made but locally on the blade. Thus "5 λ^2" term in equation 3 could be interpretated as an approximation of Glauert (*chapter 3*) power loss integrand. That being said, the extended actuator disk theory is then normally applied leading to a solvable power cubic equation in ΔV_e given as :

$$\begin{aligned}\mathcal{P}_e &= \mathcal{P}_T + \mathcal{P}_v + \mathcal{P}_{sw} \\ &= \left[V_e + (1+5\lambda^2)\frac{\Delta V_e}{2}\right]\left(V_e + \frac{\Delta V_e}{2}\right)\Delta V_e \\ &+ P_v - P_e\end{aligned} \quad (4)$$

When the above equation is solved the thrust can be computed as follows

$$F_e = \rho\pi R_e^2 \left(V_e + \frac{1}{2}\Delta V_e\right)\Delta V_e = F_e(P_e, \rho, V_e) \quad (5)$$

Finally the propeller torque is obtained by a power balance that is

$$M_e = M_e(P_e, \Omega_e) = -\frac{P_e}{\Omega_e} \quad (6)$$

A watchdog function is applied to respect the Betz limit Prandtl and Betz in windmill conditions. The latter being computed, the propeller thrust and torque can be obtained. The general momentum theory supposes the propeller to be mass and inertia less, in ASWING those properties are recovered by implementing a constant mass and angular momentum. Their expressions are not necessary for the next development (please refer to equations 94, 95, 113, 117 of Drela (2009) for more details).

P-factor model :
The EADT is extended with a P-factor model. The latter is there only to provide perturbated flow consequences on the propeller forces and moments. Coupled with a structural model, it can provide insight into whirl flutter. This model considers 2 types of perturbations, a uniform transverse velocity v, and shaft pitch rate ω depicted in figure 10. Their directions are not necessarily aligned with the engine frame axis. P-factors are computed from a simplification of the blade element theory. First of all, the local blade drag is neglected as well as the local blade aerodynamic pitch moment. Then the flow is assumed to have no slipstream angle and finally the P-factor is computed against a small perturbation assumption (ie small angles). Overall, the P-factor model returns perturbated forces and moments proportional to the transfer velocity and pitch rate perturbations. Please refer to section 14 of Drela (2008) for more details about the theoretical development. It is difficult to evaluate this model except in a whirl flutter analysis which needs a structural model (treated in the aeroelastic part of this sequel work). However, we thought that it could be interesting to see how far can go the p-factor model in non-axial flow condtion. Especially on the normal forces and yawing moments prediction in high-pitch configuration (Vertical take-off and landing configuration, VTOL). Thus only the forces and moments due to a uniform transverse velocity are briefly recalled. Let us consider that the propeller has a pitch angle α_p with the upcoming flow such as the transverse velocity seen by the propeller disk is $v = V_\infty sin\alpha_p$. The forces and moments due to the latter are given as follows

$$F_v = \frac{1}{4}\rho R^2 \left[\left(c_{l,\alpha}S_0 - c_l C_0\right)V_d + 2c_l S_1 \Omega R\right] v \quad (7)$$

$$M_v = -\frac{1}{4}\rho R^3 \left[\left(c_{l,\alpha}C_1 - c_l S_1\right)V_d + 2c_l C_2 \Omega R\right] v \quad (8)$$

where V_d is the airspeed at the propeller shaft provided by the EADT, $V_d = V_\infty cos\alpha_p + 0.5\Delta V_e$. Let cl_α be the propeller airfoil lift slope assumed constant and c_l the local lift coefficient evaluated at $0.75R_e$. The user defined coefficients C_0, C_1, S_0 and S_1 are aproximated radial blade integrand proposed by Drela. For their value please refers to *section 14.7* of Drela's work. Note that similar simplified models were proposed without omitting drag and pitch moment by Ribner, (1945b and 1945a)and *chapter 2 section 2.5* of Phillips (2004). When a propeller is under a non-axial flow it produces a normal force, yawing and pitching moments. The first 2 can be captured by equations 7 and 8 while the third is not. Thus in the evaluation section, the pitch moment is not presented, however, it must be kept in mind that ASWING can not predict it.

Jet wake and swirl modeling:
The extended actuator disk theory and p-factor model provide intels only on the propeller thrust and torque, but nothing about its jet. This gap is completed using jet and swirl models. Both are built to be consistent with the propeller thrust and moments. Jet modelling is still a modern topic, especially in hydrodynamic applications such as ship propeller efflux impact on scour. Wei et al. provide a historical review of "low fidelity" jet modelling techniques. From his work, it has been highlighted that the ASWING propeller jet model mainly derives from the Albertson et al. early work despite more recent propositions (Hong et al., Lam et al.). ASWING use also the Albertson et al.'s axial jet formulation to model the propeller swirl. This seems to be a real novelty as swirl effects are generally neglected as reported by Hong et al.. This simplification was made for hydrodynamic applications and is too conservative for aerodynamic ones, as the jet can spread a lifting surface. Both jet and swirl are thus necessary as they will significantly modify the lift distribution. That being said, the model consists of dividing the flow into two distinct zones,

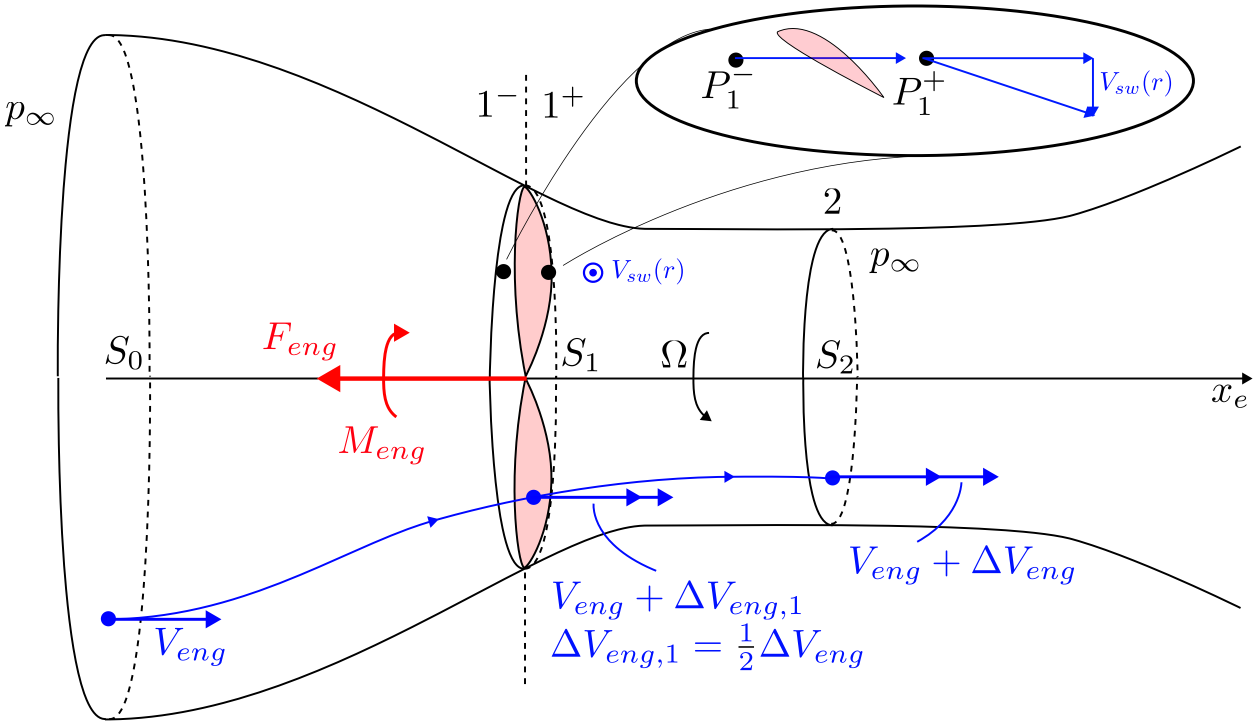

Figure 1: Extented actuator disk theory illustration

that are the Flow Establishment one (FEZ) and the Established Flow Zone (EFZ) as depicted in figure 2. Their boundaries are efflux dependent. They spread and contract linearly along the streamwise direction. Those zones are used to catch the viscous shear stress between the high and low-speed layers. The jet and swirl velocity are built as radial and streamwise coordinates functions. Their parameters are computed to be consistent with the mass flow and angular momentum conservation along the jet line. Finally, an important feature of the ASWING model, is that the jet is wind and not shaft-aligned. The jet is shed by the upcoming flow. This latter property is mainly true for high advance ratio flow. Note that the propeller hub effects are not modelled. This is discussed against a small change of the model in the evaluation section. Overall, only the propeller radius, rotation speed, and $(C_DA)_e$ are needed to model completely the jet and swirl. For more details about the jet model please refer to *section 3.4.4* of Drela (2009).

2.2 P-factor model for whirl flutter analysis:

In this section, the theoretical development of the ASWING p-factor model is proposed with a specific interest in detailing a bit more some of the assumptions and simplification made in the Drela's work. Thus the idea is to derive the blade element theory under simplifying assumption, to investigate how any perturbation seen by the shaft of the propeller has an effect on the overall forces and torques generated. No matter the perturbation at the shaft (gust, shaft bending/torsion, non-axial flow) it will always results in a perturbation in the local air relative speed $W = \sqrt{\Omega^2 r^2 + Vd^2}$ and the local flow angle $\phi = atan(Vd/\Omega r)$. V_d in the previous expressions is the propeller axial velocity defined from the EADT as $Vd = V_e + 0.5\Delta V_e$. The quantities W, ϕ and V_d are depicted in figure 3 (a) A tilde notation is adopted for the perturbed state of any variable and d for its elementary radial variation. In the ASWING p-factor model, only the lift is considered, this simplification is discussed in the evaluation section. Let us now consider that lift applied on a blade element of length dr and chord c(r) defined as

$$\begin{aligned} dL &= \frac{1}{2}\rho W(r)^2 c_l(r) c(r) dr \\ &= \frac{1}{2}\rho W^2 c_{l,\alpha}(\beta - \phi_{eff} + \alpha_0) c(r) dr \end{aligned} \tag{9}$$

Where c_l is the local lift coefficient embedding the 3D effect (swirl), the local geometric twist β and the local airfoil curvature α_0 (not shown in figure 3 -a). Now concidering a pertubation in W and ϕ denoted as $\tilde{W}$ and $\tilde{\phi}$ it comes

$$dL + \tilde{dL} = \frac{1}{2}\rho (W + \tilde{W})^2 (c_l(r) + \tilde{c_l}(r)) c(r) dr$$

Noting that the pertubated lift coefficient $\tilde{c_l}$ is given by the linear lift coefficient slope $c_{l,\alpha}$ times the pertubation angle of attack $\tilde{\alpha} = \tilde{\phi}$ Introducing into (1) it

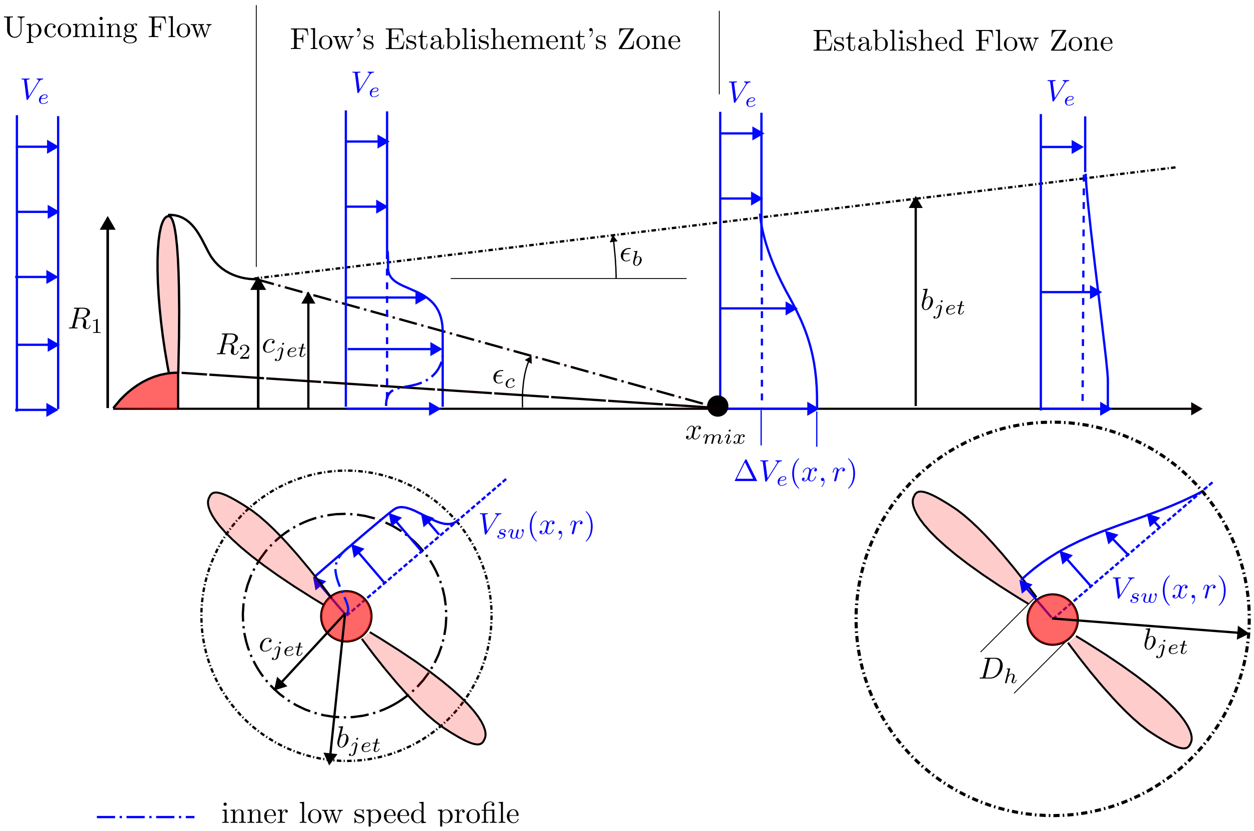

Figure 2: Jet axial and swirl velocity components used by Alderson & al and Drela with a proposed modification, an inner low speedcore is implemented to take into account the hub

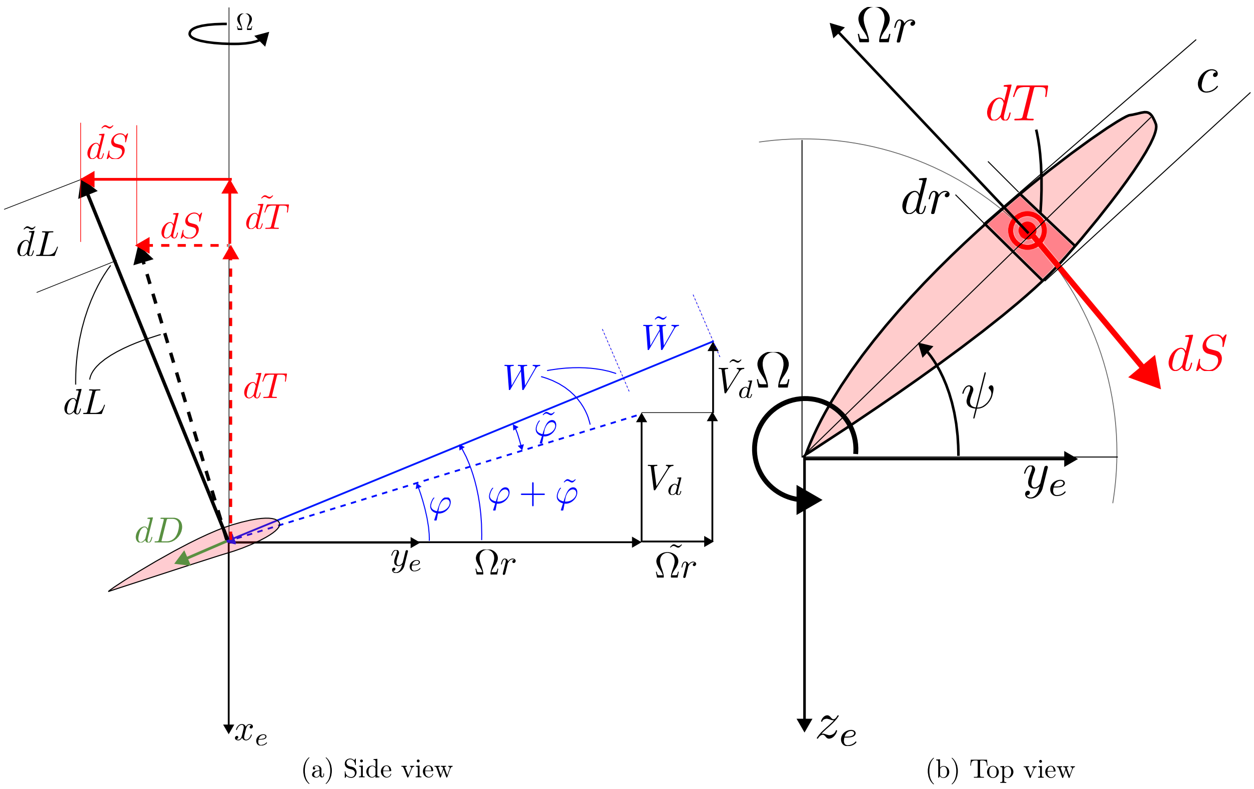

Figure 3: Elementary thrust and side force generated by a blade element. Illustration of the different perturbations

comes :

$$dL + \tilde{dL} = \frac{1}{2}\rho(W+\tilde{W})^2(c_l(r) + c_{l,\alpha}\tilde{\varphi}(r))c(r)dr$$

Developping the above expression and assuming small pertubations ($\tilde{W}W \ll 1$ and $\tilde{\phi}\phi \ll 1$), second order terms can be neglected

$$\begin{aligned} dL + \tilde{dL} &= \frac{1}{2}\rho W^2 c_l(r)c(r)dr \\ &+ \frac{1}{2}\rho\left(c_{l,\alpha}\tilde{W}^2 + 2W\tilde{W}c_l\right)cdr \end{aligned}$$

In the above expression dL can be identified using equation 9 leading to the perturbed lift expression

$$\tilde{dL} = \frac{1}{2}\rho\left(c_{l,\alpha}\tilde{\phi}W^2 + 2W\tilde{W}c_l\right)cdr \qquad (10)$$

Now let us consider, the elementary thrust and side force produced by a blade element. Those are given by convention by,

$$dT = dL\cos(\phi) \qquad (11)$$

and

$$dS = dL\sin\phi \qquad (12)$$

Now in the perturbation case, the thrust and side forces are given:

$$dT + \tilde{dT} = (dL + \tilde{dL})\cos(\phi + \tilde{\phi})$$

$$dS + d\tilde{S} = (dL + dL)\sin(\phi + \tilde{\phi})$$

Invoking small angle variation ($\tilde{\phi}/\phi \ll 1$), neglecting second-order terms, and using simplified trigonometric relations on $\cos(\phi + \tilde{\phi})$ and $\sin(\phi + \tilde{\phi})$ that are

$$\cos(\phi + \tilde{\phi}) \sim \cos(\phi) - \sin(\phi)\tilde{\phi}$$

$$\sin\left(\phi + \tilde{\phi}\right) \sim \cos\phi\tilde{\phi} + \sin\phi$$

the previous equations can be re-written as:

$$dT + dT = (dL + \tilde{dL})\left[\cos\phi - \sin\phi\tilde{\phi}\right]$$

Identifying the expression of dT (equation 11), the perturbed thrust can be isolated and expressed as:

$$\tilde{dT} = -dL\sin\phi\tilde{\phi} + \tilde{dL}\cos\phi \qquad (13)$$

Following the same for dS it leads to,

$$dS + \tilde{dS} = (dL + dL)[\cos\phi\tilde{\phi} + \sin\phi]$$

and

$$\tilde{dS} = dL\cos\phi\tilde{\phi} + \tilde{dL}\sin\phi \qquad (14)$$

Using expression of dL and $\tilde{dL}$ (equations 9 and 10) into equations 13 and 14 lead to

$$\begin{aligned} \tilde{dT} &= \frac{1}{2}\rho\Big[W^2\left(-c_{l,\alpha}\cos\phi - c_l\sin\phi\right)\tilde{\phi} \\ &+ 2W\tilde{W}c_l\cos\phi)\Big]cdr \end{aligned} \qquad (15)$$

$$\begin{aligned} \tilde{dS} &= \frac{1}{2}\rho\Big[W^2\left(-c_{l,\alpha}\sin\phi + c_l\cos\phi\right)\tilde{\phi} \\ &+ 2W\tilde{W}c_l\sin\phi)\Big]cdr \end{aligned} \qquad (16)$$

$\tilde{\phi}$ and $\tilde{W}$ in equations 15 and 16 remains unknows. They must be expressed in function of the exogenous disturbances. In ASWING only perturbation in transverse velocity v and shaft pitch rate ω are considered. As depicted in figure 4-(a), a transverse velocity v assumed uniform over the propeller disk induced a change in the local azimuthal speed as follows

$$\Omega r \rightarrow \Omega r + \partial\Omega r = \Omega r + v\cos\psi$$

where ψ is the azimuthal angle depicted in figure 4-(a). Thus $\tilde{\phi}$ and $\tilde{W}$ can be defined as partial derivatives in Ωr as follow

$$\begin{aligned} \tilde{W_v} &= \frac{\partial W}{\partial\Omega r}\partial\Omega r \\ &= \frac{\partial\sqrt{V_d^2 + (\Omega r)^2}}{\partial\Omega r}\partial\Omega r = \frac{v\Omega r\cos\psi}{W} \end{aligned} \qquad (17)$$

$$\begin{aligned} \tilde{\phi_v} &= \frac{\partial\phi}{\partial\Omega r}\partial\Omega r \\ &= \frac{\partial atan(Vd/\Omega r)}{\partial\Omega r}\partial\Omega r = \frac{-vV_d\cos\psi}{W^2} \end{aligned} \qquad (18)$$

A perturbation in the shaft pitch rate ω could occur if the latter or the wing where the propeller is attached is flexible. A pitch rate perturbation will induce a change in the local axial velocity as depicted in figure 4-(b). For small pitch range pertubation only effect on the axis can be considered. Thus the axial velocity is perturbed as follow

$$V_d \rightarrow V_d + \partial V_d = V_d + \omega rcos\psi$$

where $rcos\psi$ is the projected pitch arm as depicted on figure 4-(b). As for transverse velocity analysis $\tilde{\phi}$ and $\tilde{W}$ can be expressed as partial derivative with respect to V_d.

$$\begin{aligned} \tilde{W_\omega} &= \frac{\partial W}{\partial V_d}\partial V_d \\ &= \frac{\partial\sqrt{V_d^2 + (\Omega r)^2}}{\partial V_d}\partial V_d = \frac{-\omega V_d\cos\psi}{W} \end{aligned} \qquad (19)$$

$$\begin{aligned} \tilde{\phi_\omega} &= \frac{\partial\phi}{\partial V_d}\partial V_d \\ &= \frac{\partial atan(Vd/\Omega r)}{\partial V_d}\partial V_d = \frac{-\omega r^2\Omega\cos\psi}{W^2} \end{aligned} \qquad (20)$$

Being derived equations 17, 18,19, 20 can be injected in the elementary thrust and side force equations 15

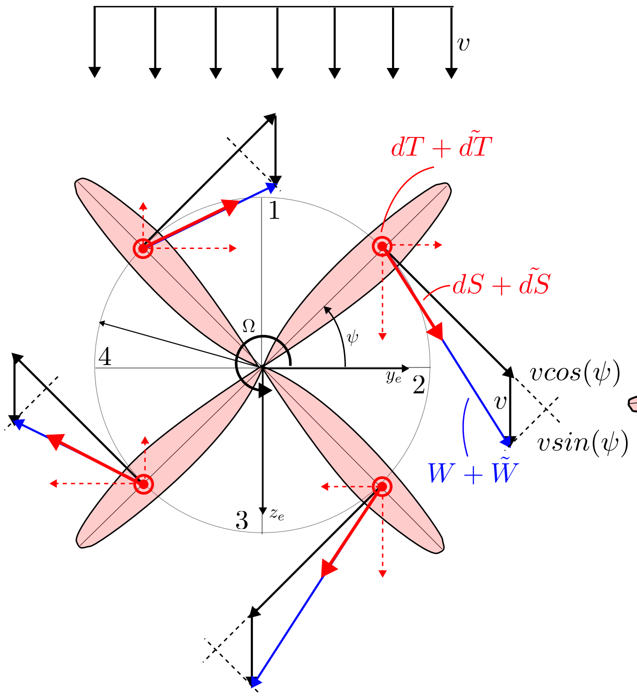

(a) A perturbation in transverse velocity v only induced a perturbation in tangential speed $\tilde{\Omega r} = vcos(\psi)$

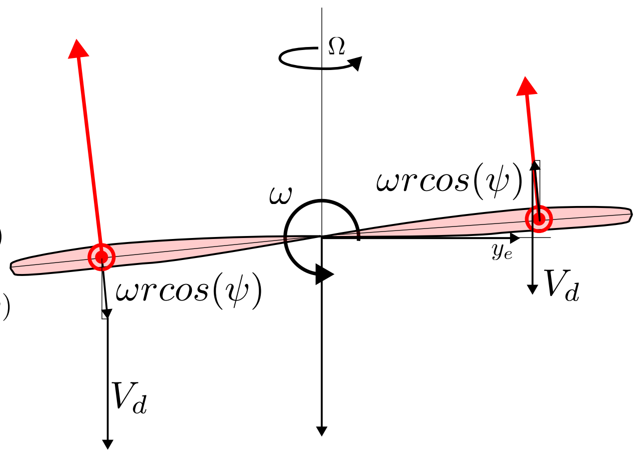

(b)Perturbation in pitch rate ω only induces a axial velocity perturbation $\tilde{V_d} = \omega rcos(\psi)$

Figure 4: Effect of perturbation in transverse velocity (a) and pitch rate (b), illustration of the assumption made in the model

and 16 leading to the contribution of v and ω to them giving

$$d\tilde{T}_v = \frac{1}{2}\rho\,[(c_{l,\alpha}cos\phi + c_l sin\phi\,)\,V_d + 2c_l cos\phi\Omega r\,]\,vcos\psi dr \tag{21}$$

$$d\tilde{S}_v = \frac{1}{2}\rho\,[(c_{l,\alpha}sin\phi - c_l cos\phi\,)\,V_d + 2c_l sin\phi\Omega r\,]\,vcos\psi dr \tag{22}$$

$$d\tilde{T}_\omega = \frac{1}{2}\rho\,[(c_{l,\alpha}cos\phi + c_l sin\phi\,)\,\Omega r + 2c_l cos\phi V_d\,]\,\omega rcos\psi dr \tag{23}$$

$$d\tilde{S}_\omega = \frac{1}{2}\rho\,[(c_{l,\alpha}sin\phi - c_l cos\phi\,)\,\Omega r + 2c_l sin\phi V_d\,]\,\omega rcos\psi dr \tag{24}$$

The dependency with the azimuthal angle can be removed by integrating the above equations over ψ. This can be in practice done if the perturbations v and ω are considered steady over a blade complete rotation. Said differently the propeller rotation speed (frequency) is assumed much greater than the bandwidth of the perturbations. If whirl flutter analysis is considered, the first 2 structural modes of the propeller shaft or the wing where it is attached, are responsible for pitching and transverse velocity. If their frequencies are much lower than the propeller rotation speed then the proposed simplification is reasonable. Before averaging it is useful to pay attention to the parity in ψ of the projected forces and moments. Let us define the pertubation frame $(x_E,\ y_v,\ z_v)$ such that $\vec{v} = v\vec{y_v}$ or $\vec{\omega} = \omega\vec{y_v}$. y_v and z_v lie into the (y_e, z_e) propeller plane. The change of frame is mandatory as the direction of the perturbation is necessarily aligned with y_E or z_E (engine frame propeller plane vectors). That being said let's consider the first time the forces generated by $\tilde{dT}$ and $\tilde{dS}$. $\tilde{dT}$ points towards x_e so is not projected, it contains a single term $cos\psi$ so will be null when averaged. The perturbated thrust does not generate any force. The elementary perturbed side force $\vec{\tilde{dS}}$ points towards the azimutal direction so must projected against y_v and z_v. When projected $\vec{\tilde{dS}}.\vec{y_v}$ contains $cos^2(\psi)$ so won't be null when averaged while $\vec{\tilde{dS}}.\vec{z_v}$ will be as it contains a $cos\psi sin\psi$ term. Thus only the side force will generate forces and will point towards the same direction as the pertubations. The same analysis must be made for moments. Let us consider the moment arm expressed in the perturbation frame $\vec{r} = r(0\ sin\psi\ cos\psi)^T$. Inspecting the cross product $\vec{r}\times\vec{\tilde{dT}}$ and $\vec{r}\times\vec{\tilde{dS}}$ 2 types of terms in ψ are identified that are $cos\psi sin\psi$ (zero when averged) and $cos^2\psi$ (non zero). It turns out that only the elementary thrust generates a zon zero moment pointing in the same direction as the perturbation. The previous comments drastically simplify the analysis. Let $\tilde{dF}$ and $\tilde{dM}$ be the elementary forces and moments. The total force and moment due to exogenous perturbations is computed by averaging the elementary forces over the azimuthal angle and integrating them over each blade as follows

$$F = \frac{1}{2\pi}\int_0^{R_e}\int_0^{2\pi}\tilde{dF}\quad and\quad M = \frac{1}{2\pi}\int_0^{R_e}\int_0^{2\pi}\tilde{dM}$$

The resulting forces and moments due to the transverse velocity or pitch rate are finally given as follows

$$F_v = \frac{1}{4}\rho R^2\,[(c_{l,\alpha}S_0 - c_l C_0)\,V_d + 2c_l S_1\Omega R]\,v \tag{25}$$

$$M_v = -\frac{1}{4}\rho R^3\,[(c_{l,\alpha}C_1 - c_l S_1)\,V_d + 2c_l C_2\Omega R]\,v \tag{26}$$

$$F_\omega = \frac{1}{4}\rho R^3\,[(c_{l,\alpha}S_2 - c_l C_2)\,\Omega R + 2c_l S_1 V_d]\,\omega \tag{27}$$

$$M_\omega = \frac{1}{4}\rho R^4\,[(c_{l,\alpha}C_3 + c_l S_3)\,V_d + 2c_l C_2 V_d]\,\omega \tag{28}$$

where C_k and S_k ($k \in [0\ 3]$) are simplified blade radial integrand involving products of the type $r^k cos(\phi)$ and $r^k sin(\phi)$. Their simplified equations are given in *equations 256-263 of section 14.7* of Drela's script and are not recalled here. Equations can be then projected in the engine frame leading to the unsteady force and torque of the propeller

$$\vec{F_e} = \begin{pmatrix} -F_e \\ F_v v_y + sign(\Omega)F_\omega\omega_y \\ F_v v_Z + sign(\Omega)F_\omega\omega_Z \end{pmatrix} \tag{29}$$

and

$$\vec{M_e} = \begin{pmatrix} -M_e \\ sign(\Omega)M_v v_y + M_\omega\omega_y \\ sign(\Omega)M_v v_Z + M_\omega\omega_Z \end{pmatrix} \tag{30}$$

3 Experimental validation

This section is dedicated to the presentation of the seven validation cases. They are summarized in the table 1 with their purposes highlighted.

3.1 CASES P 1 and 2 - Propeller thrust and torque predictions

To evaluate the extended actuator disk theory, the experimental data of Deters et al. and 2014 were used. The propeller performance measurements were performed in the 28 by 40-foot UICC open return wind tunnel. The turbulence intensity was reported to be lower than 0.1% at all operating conditions. The propeller thrust measurements were done using a T shape mechanism pendulum balance constrained by a

Table 1: Experimental evaluation cases. $\mathcal{P}$ = $\mathcal{P}$ropeller cases ; $\mathcal{AP}$ = $\mathcal{A}$erodynamics and $\mathcal{P}$ropulsion interference cases

CASE	Geometry	Exp data	Evaluation type
$\mathcal{P}$-**1**	1 RC Propeller	[3]	Static thrust against rotation speed Effect of blade number (2,3,4)
$\mathcal{P}$-**2**	2 RC Propellers	[3]	Thrust and efficiency (C_T, η) in advance flow condition
$\mathcal{P}$-**3**	1 RC Propeller	[16, 17]	Thrust and perturbation loads in non axial flow condition
$\mathcal{P}$-**4**	2 RC Propellers	[4]	Static jet and swirl velocity field (V_{xe}, V_{sw})
$\mathcal{P}$-**5**	2 RC Propellers	[4]	Jet and swirl velocity field (V_{xe}, V_{sw}) in advance flow condition
$\mathcal{AP}$-**1**	1 propeller mounted on a straight wing	[26]	Effect of a propeller jet on the wing lift distribution $c_l(y)$
$\mathcal{AP}$-**2**	1 propeller mounted on a straight wing	[26]	Effect of the propeller lateral and vertical position on the wing lift to drag ratio C_L/C_D

load cell (cf figure 5-a). 2 types of cells were used according to each propeller size to exploit the full range of the balance and ensure better accuracy. Torque measurements were fulfilled using a reaction torque sensor (RTS). Overall the C_T and C_P measurements errors were reported to be lower than 1%. Each propeller rotation speed (in RPM) was actively controlled using laser feedback. Two types of wind-tunnel corrections were applied, fairings and wind tunnel walls were captured using source distribution terms. For more details refer to *chapter 2* of Deters. Dozens of propellers have been tested in static and advanced flow conditions, in this paper, only 4 of them have been retained for thrust/torque and slipstream predictions. The DA4022 propeller in its 2, 3, and 4 blades version (9 inches) has been chosen mainly to stress out the Drela hypothesis that the "total effective blade drag area" term C_DA (equation 2) can vary linearly with the number of blades B. Specific data were also chosen to evaluate its sensitivity to the rotation rate Ω (ie Reynolds number) and advance ratio λ. Numerically, ASWING EADT has been fed with Deters et al. C_P measurements as the main idea of this evaluation is to show if for a given C_P the model provides a reasonable C_T prediction or vice et versa. As the C_P measurements are obtained by a power balance with the torque coefficient C_Q (equation 6), its prediction quality is not necessary to be studied. Figures 10 (a) and (b) present the C_T static prediction against the rotation speed. C_DA values used for the simulations are specified. Figure 10 (b) depicts the non-conservation of the C_T prediction error from the 2-blade version to the 4 one. C_DA values have been computed using a reverse formulation of the EADT from the experimental value of C_P and C_T. Figure 7-(a) gives the C_DA/B values against the rotation speed. As it can be seen, the C_DA/B curves are not exactly equal, and the mean error between the 2 blades (reference case) and the 3 and 4 versions are respectively 16 % and 22%. However, the latter does not impact as much the C_T predictions. Indeed the velocity increment ΔV_e needed to compute the thrust in the EADT is a cubic root of the power balance equation 4, while the thrust (equation 5) is a square function in ΔV_e. Thus the error due to C_DA mismatch is drastically damped leading to the witnessed small error offset from the 2 to 4 blades versions. The same conclusion can be drawn on the Reynolds number (ie rotation speed) dependency as the variation is about the same from the minimum to the maximum rotation rate. Thus considering, that the total effective blade drag area does not vary with the rotation speed and is proportional to the blade number is quite reasonable. A similar conclusion can not be drawn about the dependency with the advance ratio λ. Indeed as depicted in figure 7-(b) which presents the reverse value of C_DA based on the experimental C_T and C_P values in advance flow condition, the variation with the advance ratio are much more pronounced leading to higher predictions error, as depicted on figure 8(a) to (d). The plots present the C_T predictions for different C_DA constant values. Those are the extremum case. A trade-off could be found to minimize the error however it would be case-dependent and difficulty trackable. Instead according to the shape of C_DA variation with the advance ratio, a cost-less modification is proposed, by considering CDA as a second-order polynomial function in λ as follows:

$$C_DA(\lambda) = A_2\lambda^2 + A_1\lambda + A_0 \tag{31}$$

where the polynomial coefficients can be computed from experimental data, CFD, or other propeller codes such as QPROP for example. When implemented, the

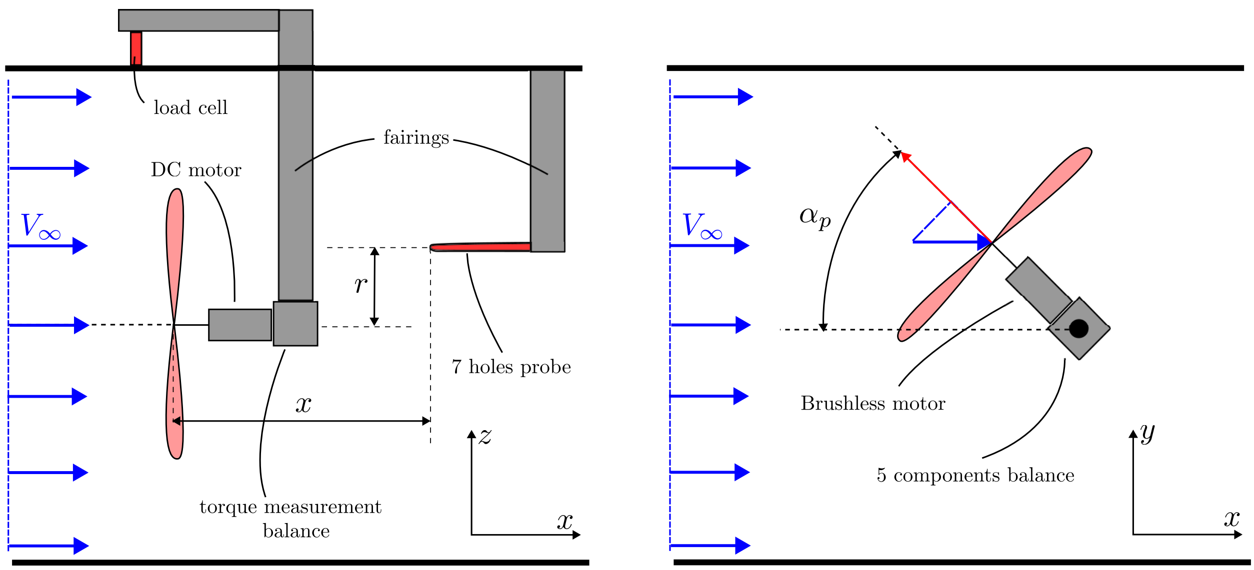

(a) Deters et al's bench (b) Leng et al's bench

Figure 5: CASE - A Experimental benches of [3] [17]

C_T predictions become better as depicted in figure 8(a)-(d) where the polynomial coefficients have been specified. The interest of the method is particularly highlighted by figures 8 (b) and (d) for the efficiency predictions. To verify the consistency of the method, the 4-blades case has been treated and the predictions are presented in figure 16 in the appendix of this paper. Similar results are witnessed. Criticisms must be made on this modification. The latter is mainly dependent on the quality of the input data. Here the $C_D A$ polynomial functions were computed based on experimental data, so the good results. The methodology will recover correctly the data that are provided. If higher fidelity CFD tools are used to compute the propeller $C_D A$ polynomial function, prediction errors are expected then but equivalent to that of the higher fidelity method.

3.2 CASE P-3 Thrust, normal force and yaw moment due to a axial flow

To evaluate the capacity of the ASWING P-factor model to predict normal forces and yaw moment due to a non-axial flow, the data from Leng Yuchen were used. The measurement was performed in 2019 in ISAE low Reynolds number wind tunnel SaBRe. The turbulence was reported to be lower than 0.1%. The propeller-motion assembly was supported by a rotating strut installed from the test section ceiling. The strut could rotate giving the propeller a pitch angle from 0 to 90° as depicted in figure 5 (b). A 5 component balance was used to measure the normal force, yaw, and pitch moments. The test bench has been validated against similar data from the literature on a Graupner E-prop. The bench was reported as qualitative. The author provided in Leng et al. (2019 and 2020) the thrust, torque, normal force, yaw, and pitch moments coefficient. The latter was given as a function of the propeller pitch angle α_p and advance ratio λ_∞. Note that the ASWING P-factor model can not predict the pitch moment due to non-axial flow. Thus only the normal force, yaw moment, and thrust coefficients (C_N, C_n, C_T) predictions are presented. A NACA propeller was used with a linear blade pitch varying. The geometry is provided in *Appendix A* of Leng Yuchen's script. The blade tip pitch angle and airfoil are respectively 20° and NACA0012. The propeller size ($R_e = 0.85m$) was chosen as a tradeoff between minimal wall interactions and 3D printing quality.

Figure 9 (a)-(c) presents the normal forces, yawing moments, and thrust coefficients ASWING predictions. The latter are compared to Leng et al.'s experimental data and non-linear model. The coefficients are given against the propeller pitch angle α_p (cf figure 5-b) for different advance conditions ($\lambda \in [0.2,\ 0.45,\ 0.7,\ 1.0]$). As expected from the small angle assumption of the model, ASWING is not able to predict the yawing and normal force coefficient accurately, on $\lambda = 0.2$ seems to show interesting agreements at low pitch angle but is still far beyond Leng et al.'s non-linear model accuracy. This is consistent with Leng Yuchen's *chapter 2* observations on lower advance-ratio and pitch angle on a close linear model. Moreover, as the blade drag contributions are not taken into account, the model loses the track after a pitch angle superior to 45° when the drag contributions become dominant. From this comparison and the data of Leng Yuchen (*chapter 3*), a validity map

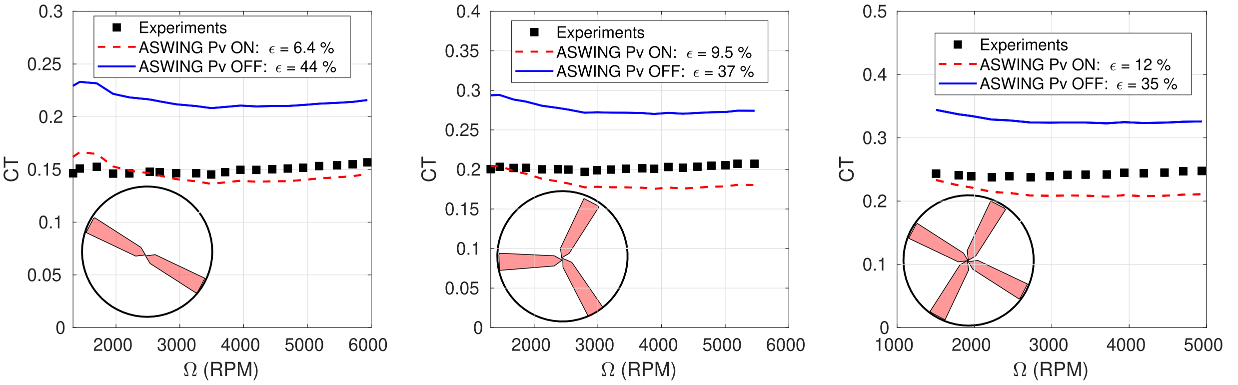

(a) 2 Blades ($C_DA = 1.6\ 10^{-4}m^2$) (b) 3 Blades ($C_DA = 2.4\ 10^{-4}m^2$) (c) 4 Blades ($C_DA = 3.2\ 10^{-4}m^2$)

Figure 6: CASE $\mathcal{P}$-1 Static thrust coefficient ASWING prediction for the DA4022 propellers, comparison between the 2, 3 and 4 blades versions. ϵ is the mean error between predictions and experiments

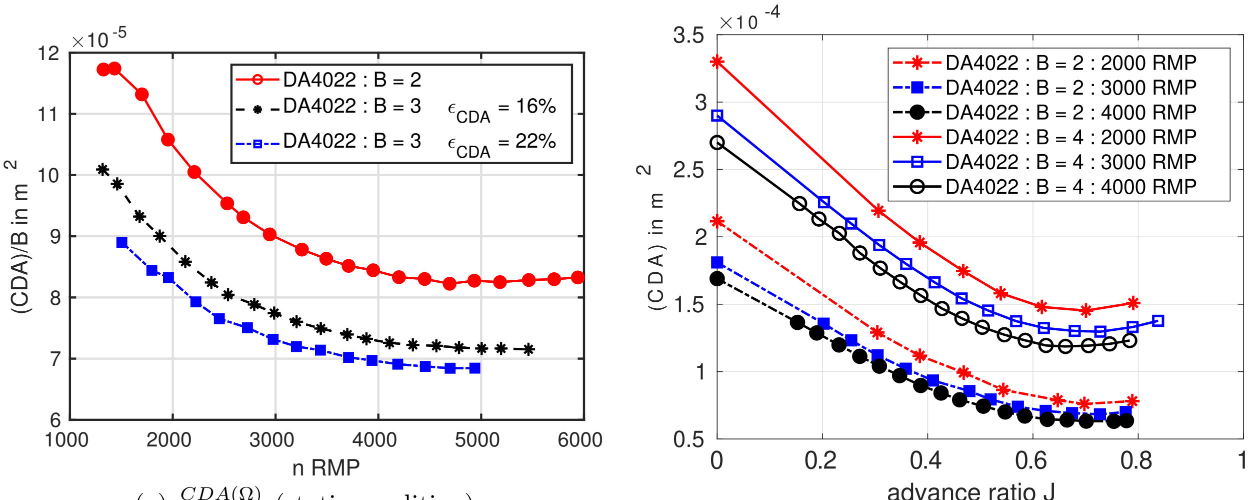

(a) $\frac{CDA(\Omega)}{B}$ (static condition) (b) $CDA(\lambda, \Omega, B)$

Figure 7: CASE $\mathcal{P}$-1 C_DA reverse computation from experimental data in static and advance flow condition. Effect of B, Ω and λ. ϵ_{CDA} is the mean error between C_DA value of the 2 blades version and the other one

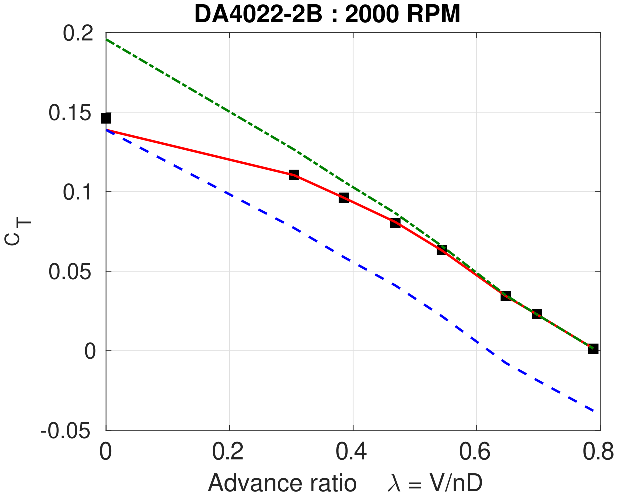

(a) C_T at 2000 RPM

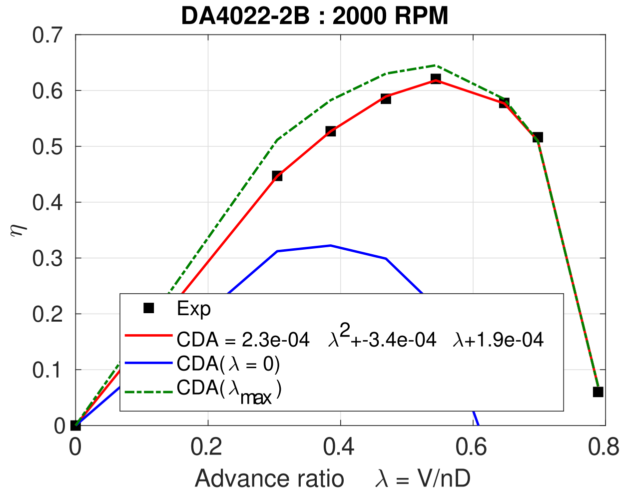

(b) η at 2000 RPM

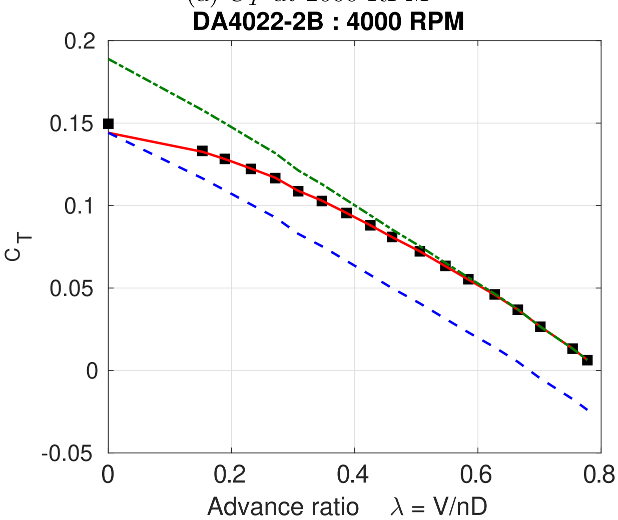

(c) C_T at 4000 RPM

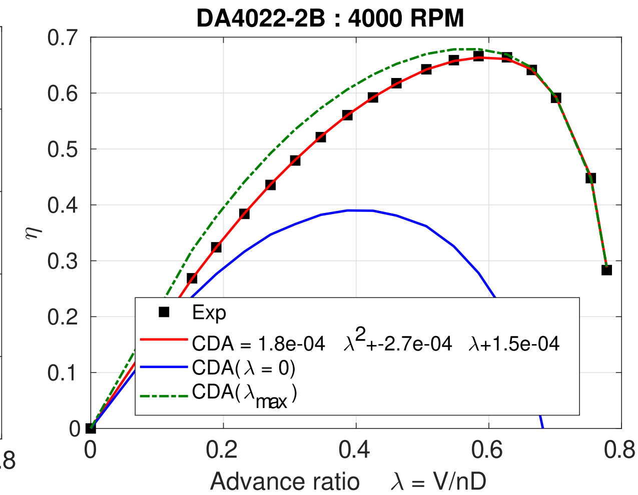

(d) η at 4000 RPM

Figure 8: CASE $\mathcal{P}$-2 Advance flow : C_T and η ASWING predictions for the DA4022-2B, comparison with rotation speed. Performance improvement with C_DA defined as a polynomial function of the advance ratio λ. The value λ_{max} corresponds to $C_T(\lambda_{max} = 0/0$

in α_p and λ could be built and is depicted in figure 10. The dark grey represents the set of parameters where the P-factor model is considered satisfying. Despite those latter bad predictions, this model remains interesting for whirl flutter analysis that is presented in the aeroelastic part of this sequel work. Here the objective was to build and identify the boundaries of the p-factor model for flight mechanics analysis.

As Leng et al. provided C_T and C_P measurements in the function of the pitch angle α_p and advance ratio λ, the EADT could be benchmarked against Leng et al.'s non-linear model in non-axial flow condition. To do so a quadratic C_DA in μ was used where μ is the shaft advance ratio defined as $\mu = \lambda cos\alpha_p$. The polynomial coefficients are provided in figure 9-(c) legend. It turns out that the ASWING modified EADT model shows excellent agreements with experiments until 60° no matter λ. After that, Leng et al.'s non-linear model becomes better.

3.3 CASE P 4 and 5 Propeller slipstream measurements

The jet slipstream predictions are evaluated against Deters et al. and Deters (2014 *chapter 8*) experimental work. The same bench (figure 5-a) as depicted in the thrust prediction section was used. A 7 hole probe has been used to measure the axial and swirl velocities. Its position could vary vertically and horizontally (cf figure 5-a). According to Deters et al., measurements on the complete propeller disk were not necessary from the axisymmetry property of the flow. Each measurement slice was spaced by 45 cm. The maximum streamwise and radial coordinates of the probe to the propeller centre were respectively 3.0 and 1.5 propeller diameter. Each probe hole was connected to a series of MKS pressure transducers giving an accuracy of 0.06 m/s and 0.9° for axial velocity and angle of attack. The measurement errors were reported as small enough to be not plotted in the author's publication. The data have been digitalized using webplotdigitalizer. Several propellers at different rotation rates and advance flow have been used to evaluate the jet model. In this paper, the GWS APC and DA4002 results are presented. Their geometries are depicted in figure 17 in the appendix of this paper. Axial and swirl velocity predictions are presented in static and advanced flow conditions. For the static one, the engine jet model was reproduced in MATLAB while in advanced flow conditions, a numerical bench was set up in ASWING. Axial velocities and angle of attack were provided by the numerical sensors at each streamwise and radial position. The swirl velocity was reconstructed using the local angle of attack or side slip angle measurements combined with the axial velocities.

That being said, the figures 11 (a) and (b) present the static axial and swirl velocity predictions against Deters et al. experimental data on the GWS propeller. A single rotation rate ($\Omega = 5000RPM$) is presented. Five normalized streamwise locations are presented ($\frac{x}{D} \in [0.125,\ 0.5,\ 1.0,\ 3.0]$). For the axial velocity, a general trend can be observed, ASWING is weak near the propeller plane ($\frac{x}{D} < 0.5$) to show good agreements while satisfying one is witnessed after. Similar observations are done on the swirl predictions (figure 11 -b). Those discrepancies are mainly due to the propeller hub which does not accelerate the fluid, thus a low-speed region is observed for small radial positions. In consequence a modification has been proposed to take into account those effects. A low-speed region has been implemented as depicted in figure 2. Its diameter tends to reduce linearly with the streamwise distance until the mixing point. The velocity profile is constructed to be consistent with the other regions. This modification is denoted as ASWING-m. From figure 11 (a), the modification improves a bit the axial and swirl velocities predictions at $\frac{x}{D} = 0.125$. The benefit tends to lower for greater spanwise locations. Another propeller (APC at 9000 RPM) was used to robustify the analysis. Predictions results are presented in figures 18 (a) and (b). This case contradicts the previous observations, especially on the swirl predictions near the propeller blade. Indeed the ASWING unmodified version shows better agreements with experiments. For axial velocity, ASWING-m remains better. Also using 2 propellers as static validation case are of interest to highlight the difference in velocity profile because of each propeller geometry. This change is not captured by ASWING nor its modified version. However, they both capture quite well the jet spreading and the ZEF and EFZ boundaries.

Figure 12(a) and (b) presents predictions in advance flow condition ($\lambda = 0.52$) on the GWS propeller at a rotation speed of 5000 RPM. A large low-speed profile ($r/R < 0.25$) is not captured by both models. Also a negative swirl velocity zone (cf 12-b) is observed for streamwise location ($x/D = 0.125$ and $x/D = 0.5$) and is not captured. For downstream locations, ASWING-m shows better agreements. Again by studying another propeller (DA4002 at 5000RPM and $\lambda = 0.64$), depicted in figure 19 in Appendix, contradicting results are observed. Indeed, ASWING shows better performances than ASWING-m no matter the streamwise location on the swirl velocity predictions. For axial velocity, ASWING-m remains better. In light of the results, both ASWING jet models show reasonable agreements with experiments for axial and swirl velocities predictions for $\frac{x}{D} >= 0.5$. Lower

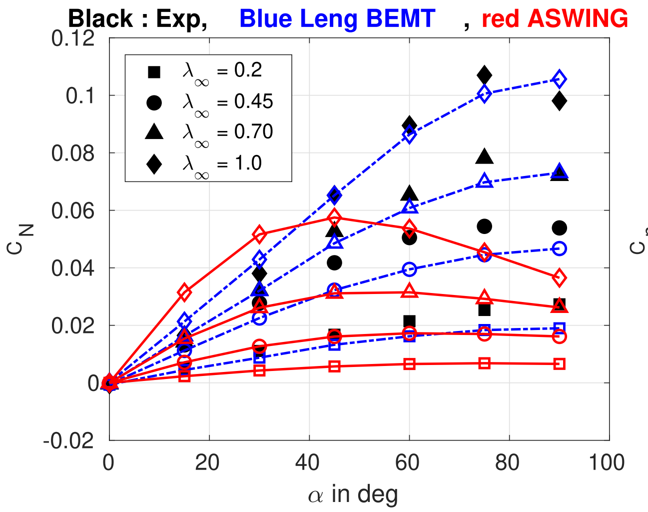

(a) Normal force coefficient C_N

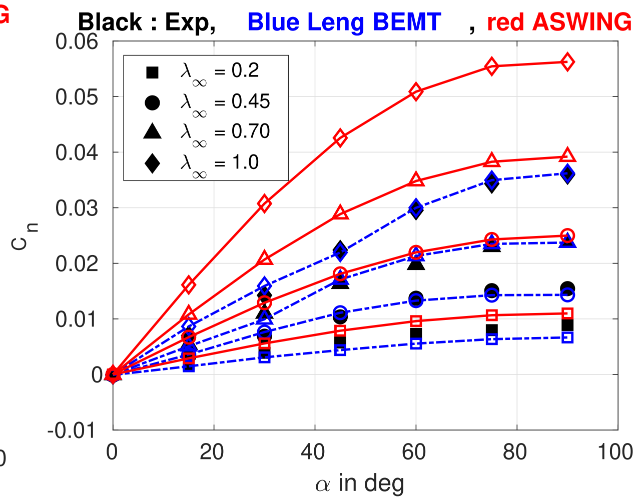

(b) Yaw moment coefficient C_n

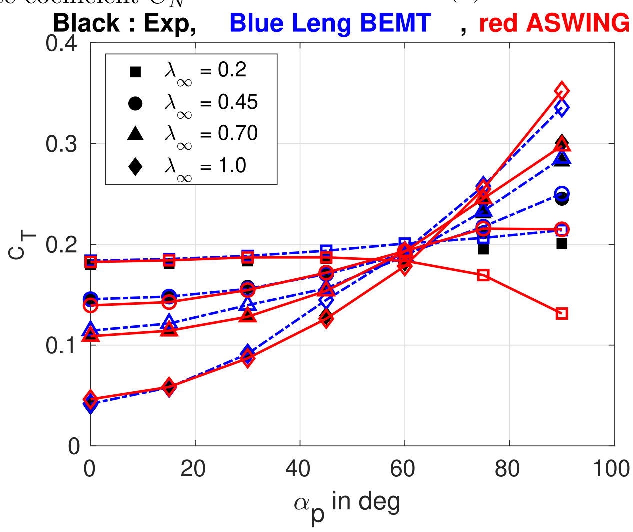

(c) Thrust coefficient C_T
with $C_D A(\mu) = 0.0019\mu^2 - 0.0026\mu + 0.0006$

Figure 9: CASE $\mathcal{P}$-3 Normal force, Yaw moment and thrust coefficient ASWING's predictions comparison with experiments from Leng et al..

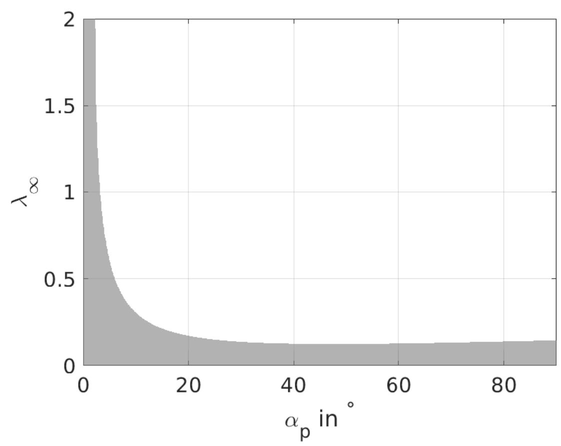

Figure 10: $\mathcal{L}_{\tilde{W},\tilde{\phi}}(\alpha_P, \lambda_\infty)$ small pertubation validity map

performances are reported for swirl computations on both models. Better performances are witnessed on ASWING-m only for axial velocity predictions. Finally, prediction errors must be commented on. A swirl velocity will induce a local change in the angle of attack. Local lift varies linearly (in unstalled region) with the angle of attack while it does quadratically with the axial velocity. As the swirl velocity induces a change in the local angle of attack, its prediction error is weightless in comparison to the axial velocity. Predictive performances can be considered equivalent.

3.4 CASE AP-1 Propeller slipstream/lifting surface interaction

In this last evaluation section, the capacity of ASWING to predict the interactions between a propeller jet and a wing is investigated. To do so, the experimental data of 2 benches were used from the work of Veldhuis (*chapter 5*), Veldhuis (1996 and 2004). The first one named PROWIM had the purpose of highlighting the effect of a propeller jet on the lift distribution while the second (APROPOS) aimed at providing insight into the propeller spanwise and vertical position effect and the lift/drag ratio of the wing. No matter the bench, the tests were performed in the 1.8 X 1.25 m Delft University Low Turbulence Tunnel. The wind speed was 50m/s for both benches. The level of turbulence was 0.025%. The same wing was used on PROWIM and APROPOS that was straight with a smoothed tip as depicted in figure 13. The wing chord and half span were 0.24 and 0.64m (AR = 5.3) and the airfoil was a NACA642-A015. Strips were placed on the intrados and extrados to force the boundary layer transition at 30 % of the chord. Several monitoring devices were used but only are of interest in this paper, a 6-degree of freedom balance to measure the total lift and drag coefficient and 20 pressure tape rows to measure the local lift coefficient. The latter were wisely placed to refine the pressure measurement near the propeller axis (cf figure 13-a).

Numerically, the first bench was reproduced without the airframe where the propeller is connected. Its spanwise, streamwise, and vertical coordinates are respectively $x_p = -0.23m$, $y_p = 0.3m$, and $z_p = 0.0m$. The airfoil polars were computed in XFOIL at the given Reynolds number condition (800 000) and the n_{crit} was adjusted to ensure the transition of the boundary layer around 30% of the chord. The NACA642-A015 lift linear slope is then $c_{l,\alpha} = 5.72$. The maximum lift coefficient and zero lift angle of attack are respectively $c_{l,max} = 1.2$ and $\alpha_0 = 0.0°$ while the profile drag coefficient was set to $c_d = 0.0635$. The propeller was turning at the same rate in both benches ie $\Omega = 500 rad/s$. The latter was not provided by the author but has been computed from the propeller tip Reynolds number and the advance ratio. The propeller blade drag area was set to $(C_D A) = 4.4874e - 04\ m^2$. The propeller thrust coefficient and advance ratio of the PROWIM bench were set to $C_T = 0.168$ and $\lambda = 0.85$ while the APROPOS were $C_T = 0.120$ and $\lambda = 0.92$. From those values, the shaft power was computed to match the latter values and injected in ASWING avoiding accumulating errors from the EADT.

Figure 14 depicts the ASWING predictions for the first bench (PROWIM). Three different angles of attack were evaluated ie $\alpha = 0,\ 4,\ 10°$ and 2 rotation directions (ClockWise and Counter-ClockWise, CW and CCW). For the data used in the figure 14 ASWING is compared to the work of Goates who implemented a different propeller jet model and a less sophisticated lifting line one. From figure 14, ASWING predicts in good agreement with experiments the lift distribution for $\alpha = 0.0°$ and $\alpha = 4.0°$. Moreover, it performs better than Goates's model. At $\alpha = 10°$, both models seem weak to predict the lift distribution near the propeller axis. ASWING shows better lift predictions than Goates's model outside the propeller disk but it is out of this article's scope. Finally from figure 14 (b) where the rotation direction is inverted (Counter-ClockWise), the same remark can be made on the accuracy of ASWING at a low angle of attack. In both figures, some discontinuities can be witnessed in the ASWING lift distribution. This is not due to a coarse mesh but to the inversion of the swirl velocity direction at the propeller axis, inducing a sudden change in the angle of attack. The discontinuity around the propeller disk boundary is due to the steepness of the jet velocities profile as illustrated for example in the figures 12(a) and (b).

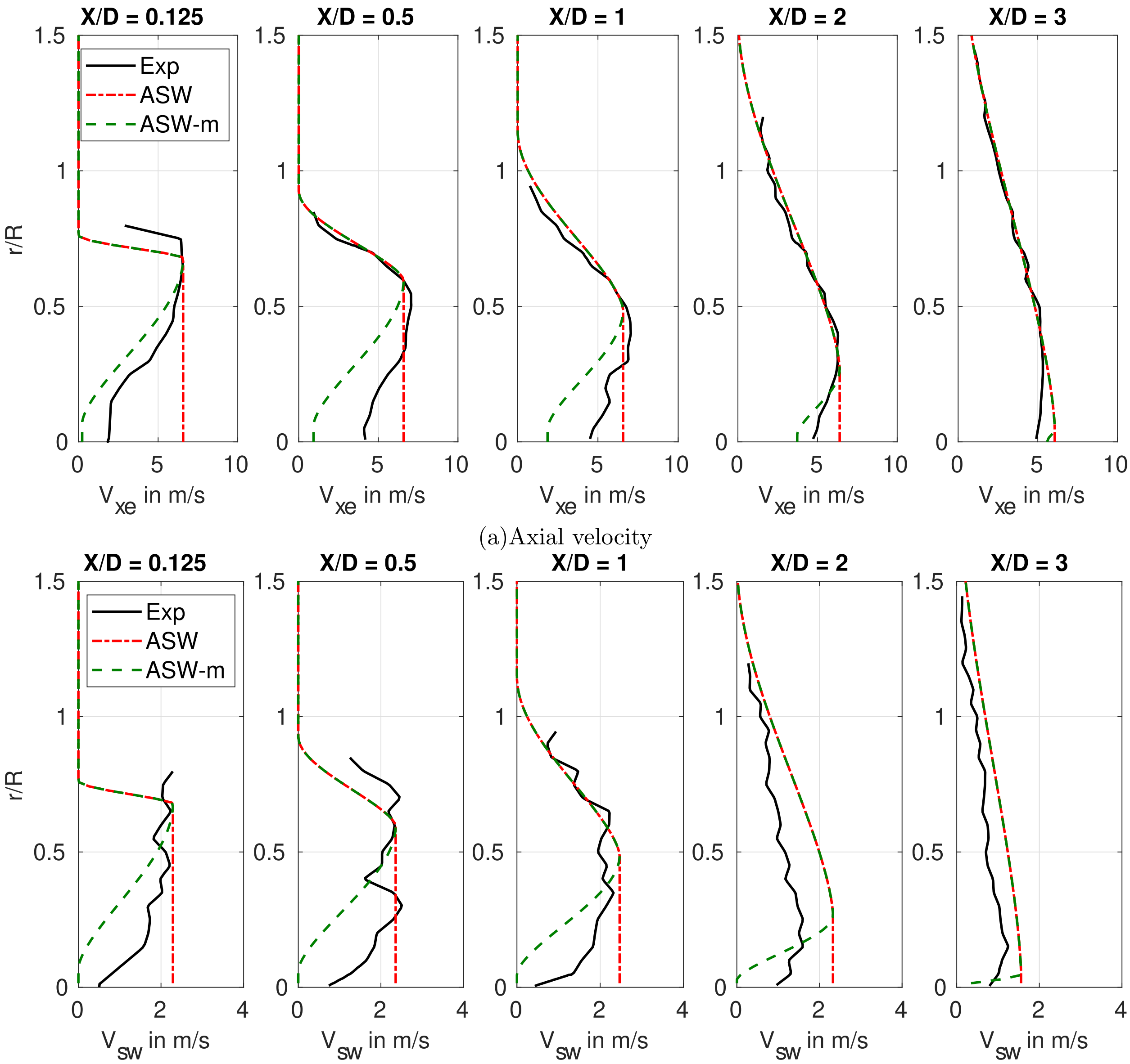

(a)Axial velocity

(b) Swirl velocity

Figure 11: CASE $\mathcal{P}$-4 Static GWS (5000 RPM) axial and swirl velocities evaluated at different streamwise location $\frac{x}{D}$ and different radial position $\frac{r}{R}$ (y-axis). Comparison of ASWING 5.96 and ASWING-m predictions with experimental data from Deters et al. (2015)

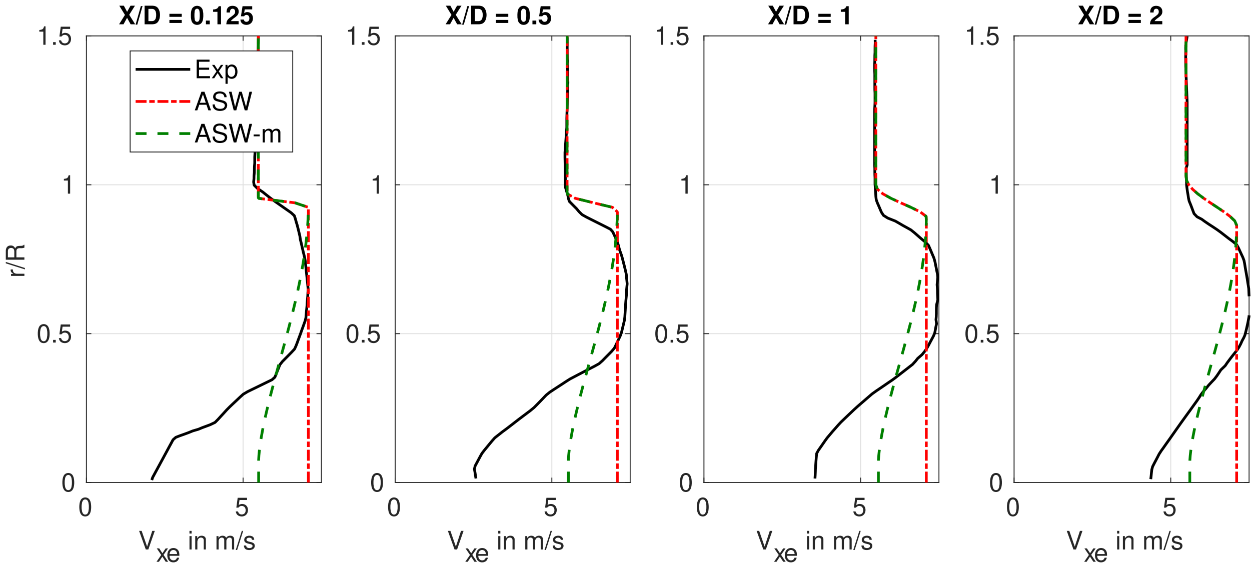

(a)Axial velocity

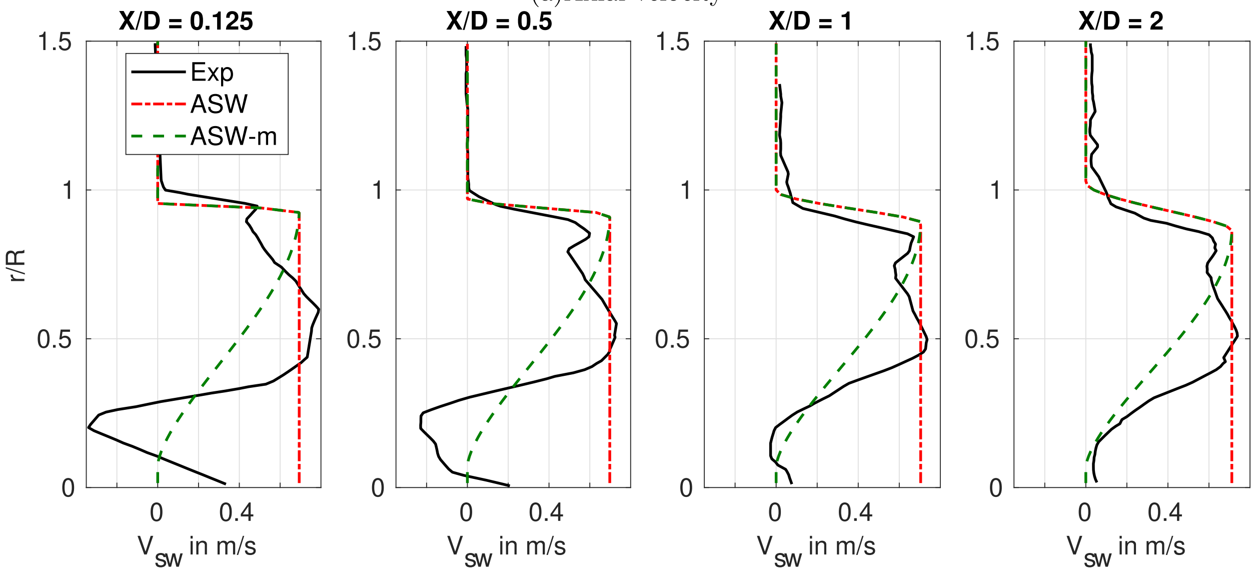

(b) Swirl velocity

Figure 12: CASE $\mathcal{P}$-5 Advanced flow GWS (5000 RPM), $\lambda = 0.52$, axial and swirl velocities evaluated at different streamwise location $\frac{x}{D}$ and different radial position $\frac{r}{R}$ (y-axis). Comparison of ASWING 5.96 and ASWING-m predictions with experimental data from Deters et al. (2015)

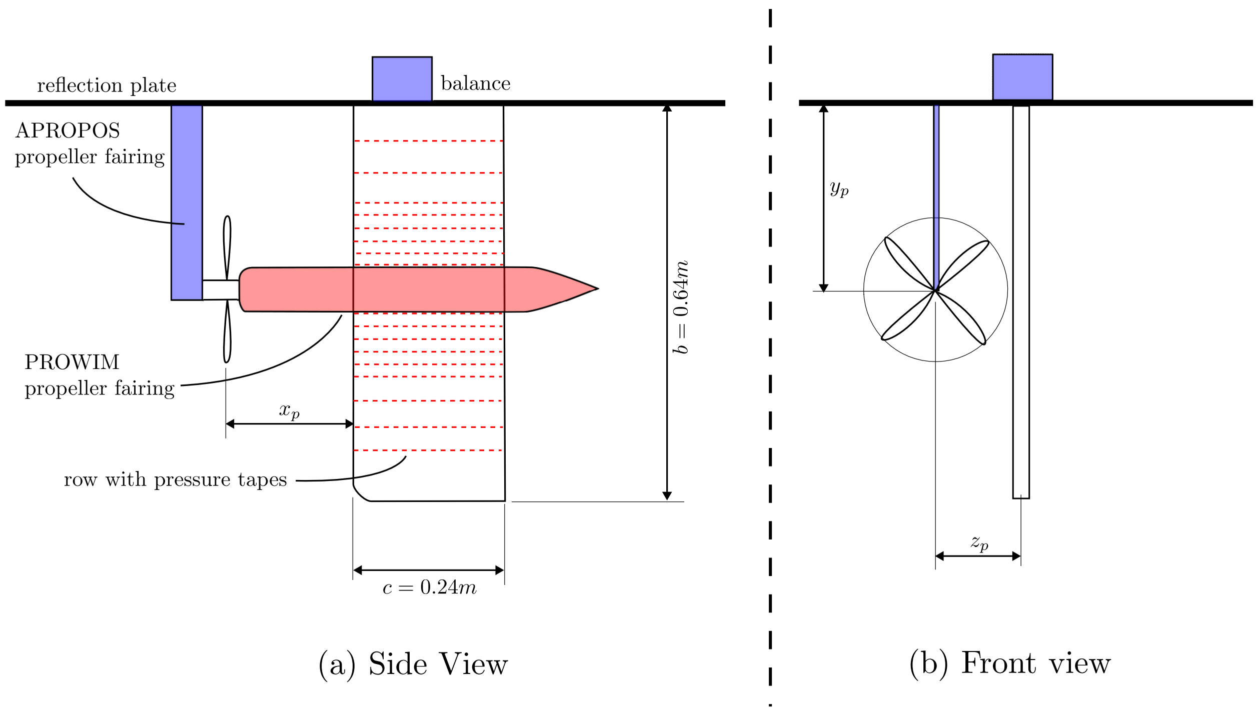

Figure 13: CASE $\mathcal{AP}$1-2 Veldhuis PROWIM and APROPOS experimental benches

The figures 15 (a) and (b) depict the ASWING predictions of the impact of the propeller spanwise and vertical position (y_p and z_p) on the lift over drag ratio. 2 angles of attack were tested ie $\alpha = 1.05°$ and $\alpha = 4.2°$. In both positions, 5 vertical positions were tested and for each of them, 13 spanwise locations were chosen. The propeller spanwise location could not start from 0.0 because of physical constraints with the wind tunnel walls. In figure 15 (a) and (b) the black markers indicate experimental data while the red one indicates ASWING predictions. Marker type indicates the vertical position of the propeller. Also in blue is displayed the lift drag ratio value if the propeller is off (ASWING only). The same conclusions can be drawn from both figures. ASWING is not capable of capturing the effect of the vertical position on the lift-drag ratio. This comes from the ASWING lifting line model. The lift and drag are computed based on the air relative velocity computed at the quarter chord location. This implies a vertical uniform flow. Or as reported by Veldhuis 2005 (in *section 5.5.2*) the increase in lift drag ratio when the propeller axis is placed above the wing is due to an increasing speed on the wing leeward ie a loss of pressure leading to a rise in the lift. The effect is the opposite when the propeller axis is placed below the wing. Figure 15 (a) and (b) do highlight a capture of the vertical position, however, it does originate in the above physical insight. The propeller jet and swirl regardless of the rotation direction drastically modify the lift distribution leading to greater lift-induced drag than if the propeller was off. When the propeller is moved vertically, the axial and swirl velocities decrease with the vertical position modifying less in consequence the lift distribution and thus the induced drag. That being said when only the neutral vertical position ($z = 0$) is considered, ASWING captures well the effect of the propeller spanwise position on the lift drag ratio ie an increase with it towards the wing tip. When the propeller direction is clockwise the swirl velocity tends to oppose the wing tip vortices reducing the lift-induced drag of the wing. When the propeller turns in a counterclockwise direction (not shown), Veldhuis (2005) witnessed a decrease of performance. Similar conclusions were drawn from ASWING analysis.

Final remarks must be made on the capture of the slipstream deviation due to the jet wing interaction. Veldhuis provided in his work a wake survey of the PROWIM bench for clockwise rotation. He identified a slipstream deformation. The propeller jet disk was split by the wing in 2 half disks, the upper one shifted toward the wing root and the lower down in the opposite way. The shift length was around 20% of the propeller radius. This phenomenon was also witnessed and investigated experimentally in static flow conditions by Deters et al., [3] (*chapter 8*), Leng et al., [17] (*chapter 4 and appendix D*). In the case of the PROWIM the non-zero lift outside the propeller disk in 12(a) at $\alpha = 0°$ indicates a non-zero circulation ie vorticity. Thus the resulting velocity field from the horseshoe systems of the wing tends to spread the propeller jets. However, it is quite difficult to quantify the half-disk shift. Moreover, if other lifting surfaces are placed more downstream it is very unlikely to catch correctly the effect of the spread jet on the lift distribution. So it is not recommended to use ASWING for such applications.

4 Conclusions:

This technical report has presented an experimental evaluation of the ASWING propeller model. Some of the assumptions of the extended actuator disk theory (EADT) have been discussed and some modifications have been proposed. Here is a summary of the different findings:

- When extended, the EADT shows good agreements with experiments on several propellers in static and advanced flow conditions. ASWING can directly provide the propeller shaft power needed to trim an aircraft in a given situation (steady level or banked flight).
- The p-factor model mainly used for whirl flutter analysis is not able to predict normal force and yawing moments due to a non-axial flow because of its small perturbation assumption. A logical map in advance ratio and pitch angle has been provided where the model is expected to behave reasonably well. However, the use of ASWING for V-TOL configuration (high pitch) is not yet recommended.
- Contrary to the normal and yaw moments, the modified EADT shows good agreements with experiments for thrust coefficient predictions in non-axial flow conditions up to $\alpha_p = 60°$. ASWING will capture in consequence the effect of small side slip and angle of attack on the propeller performances.
- Then the jet and swirl model and its modification proposed show good agreements with experimental data on several propellers in advance and static flow conditions. The predictions become better when the flow is evaluated at a downstream distance greater than half the propeller diameter.
- Finally, propeller jet wing interactions have been presented. ASWING is capable of capturing the effect of a propeller jet on the wing lift distribution no matter the rotation direction. Plus it can capture the effect of the spanwise location of the propeller on the wing lift drag ratio. However, it can not be for the vertical position influence as it involves a fluid mechanism not captured by ASWING (different upcoming speeds on leeward and windward sections).

5 Appendix - A : Complementary data, and propellers geometries

This appendix presents additional experimental comparison with ASWING predictions. Figures 16 (a) to (d) present extra validation of the extended actuator disk theory one DA4022 propeller at 2 different rotation speeds. Figures 17 (a) to (d) present the the propellers geometries. Figures 18 (a) and (b) present an additional validation of the jet and swirl models in static condition on the APC propeller at 9000RPM. Finally 19 (a) and (b) highlight the same validation but in advance flow condition.

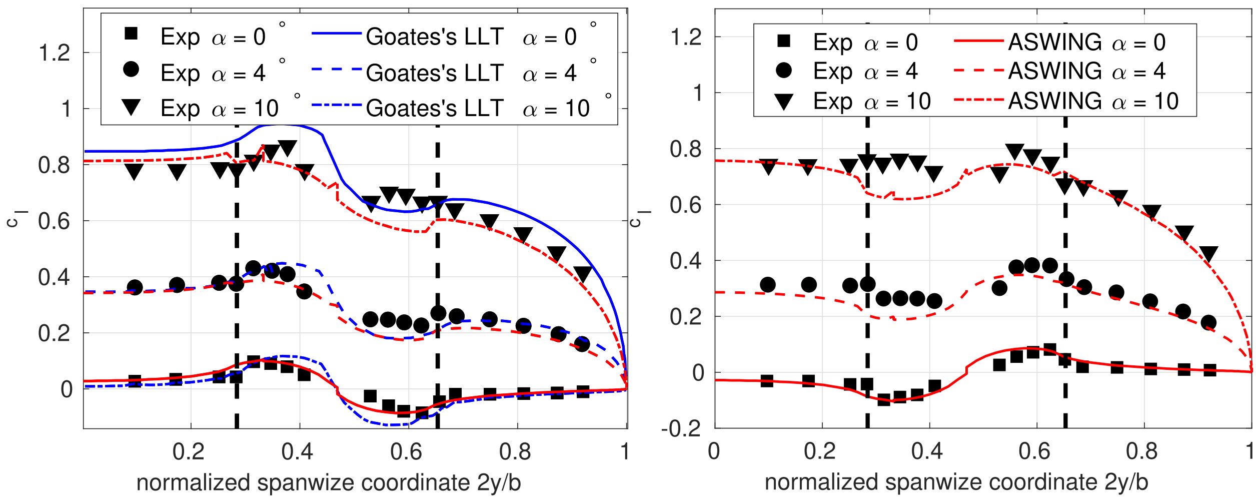

(a) clockwise (b) counter-clockwise

Figure 14: CASE $\mathcal{AP}$-1 Jet wing interaction, effect on the lift distribution, comparison with Goates's jet and non-linear lifting line theory model. Experimental data from PROWIM bench of Veldhuis

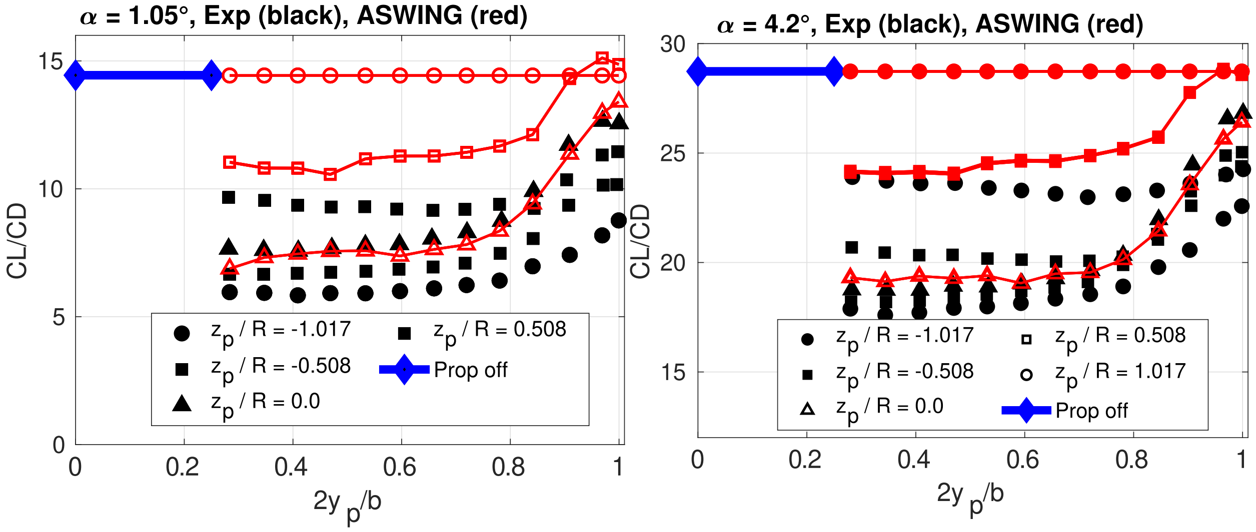

(a) $\alpha = 1.05°$ (b) $\alpha = 4.2°$

Figure 15: CASE $\mathcal{AP}$-2 Effect of the spanwise and vertical position of the propeller on CL/CD ratio. Aswing prediction versus Veldhuis's experiments (bench APROPOS)

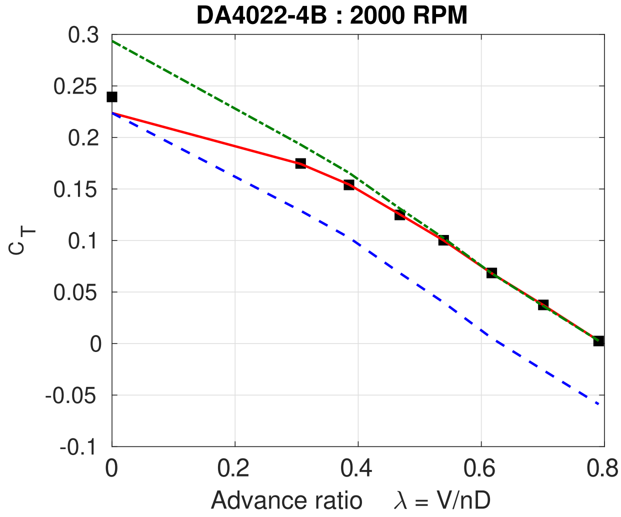

(a) C_T at 2000 RPM

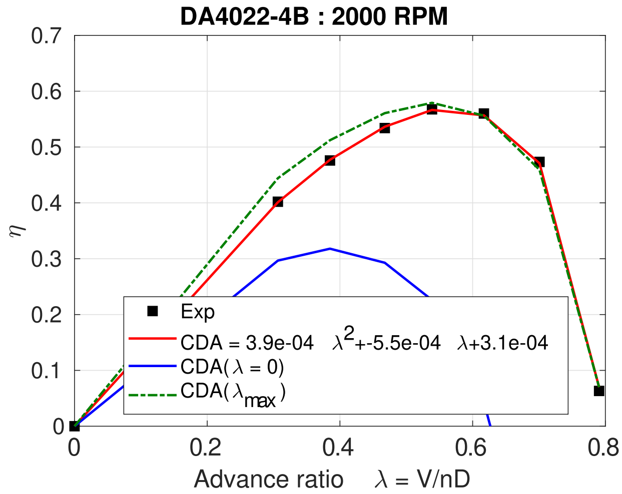

(b) η at 2000 RPM

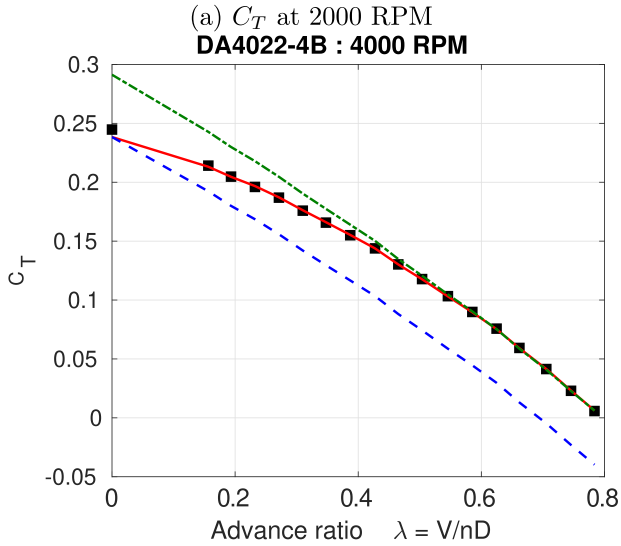

(c) C_T at 4000 RPM

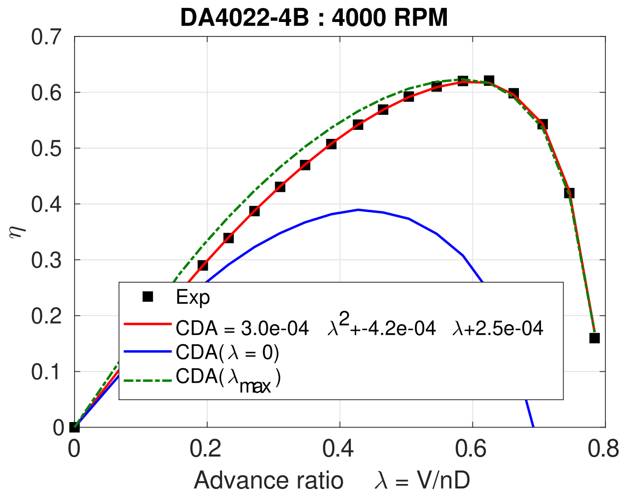

(d) η at 4000 RPM

Figure 16: CASE - A Advance flow : C_T and η ASWING predictions for the DA4022-4B, comparison with rotation speed.

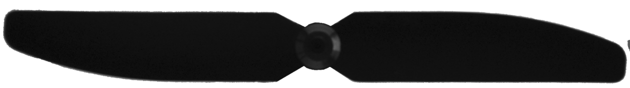

(a) GWS 5X4.3

(b) APC Sport 4.2X2

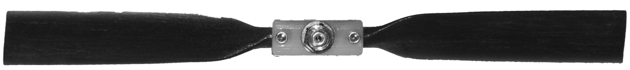

(c) DA4002 9 in

(d) DA4022 9 in

Figure 17: Propellers used for thrust, power, axial jet and swirl predictions (CASE A and C)

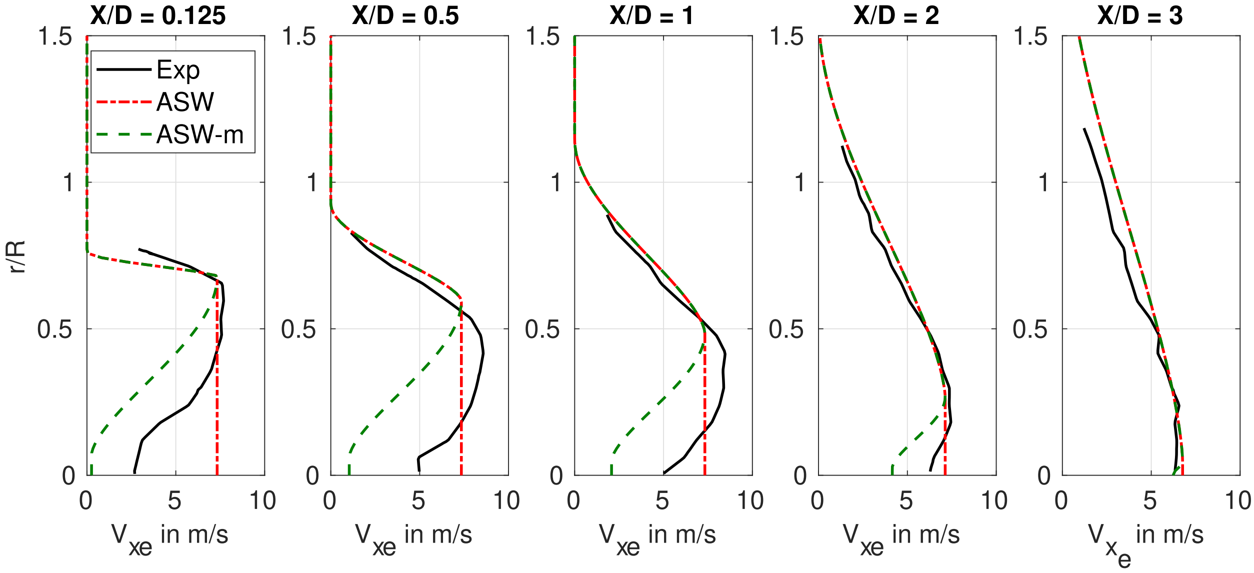

(a)Axial velocity

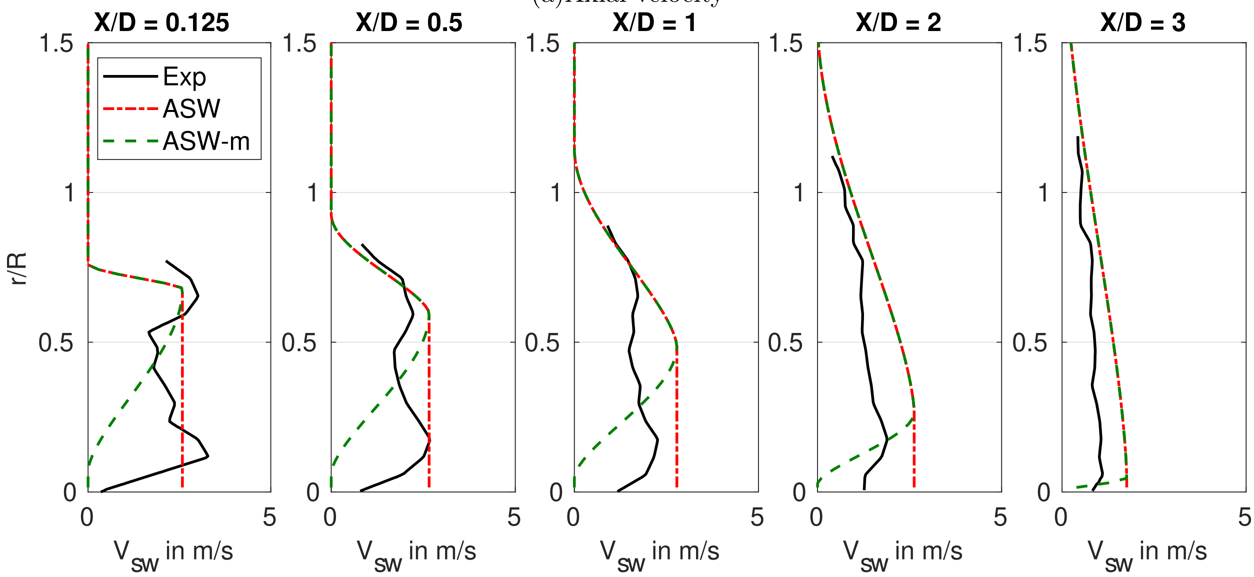

(b) Swirl velocity

Figure 18: CASE - C Static APC (9000 RPM) axial and swirl velocities evaluated at different streamwise location $\frac{x}{D}$ and different radial position $\frac{r}{R}$ (y-axis). Comparison of ASWING 5.96 and ASWING-m predictions with experimental data from Deters

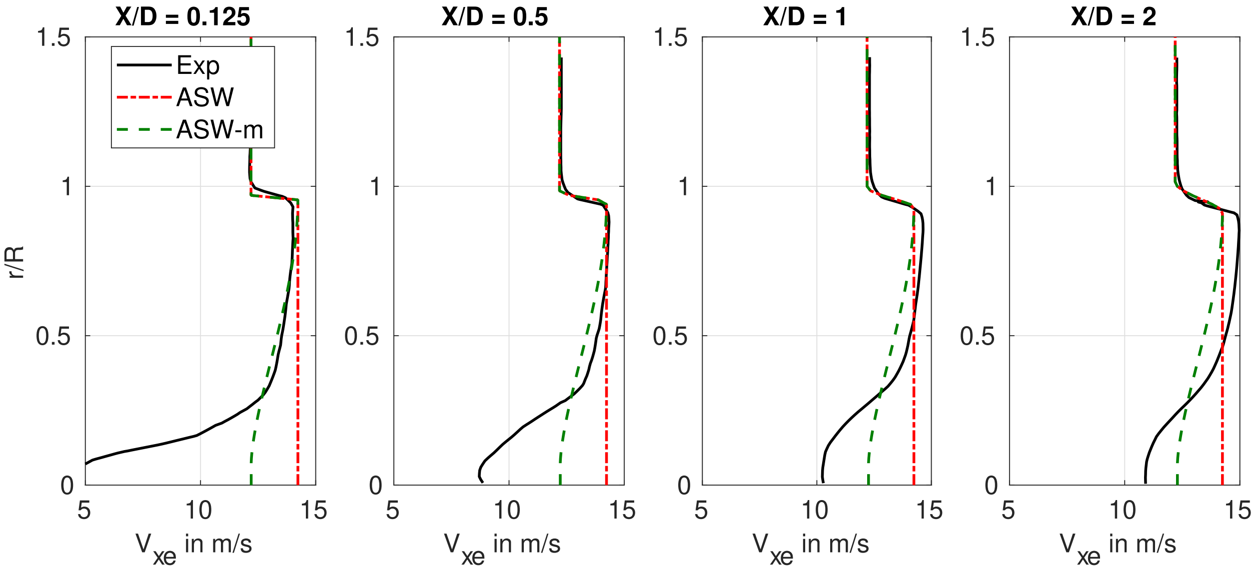

(a)Axial velocity

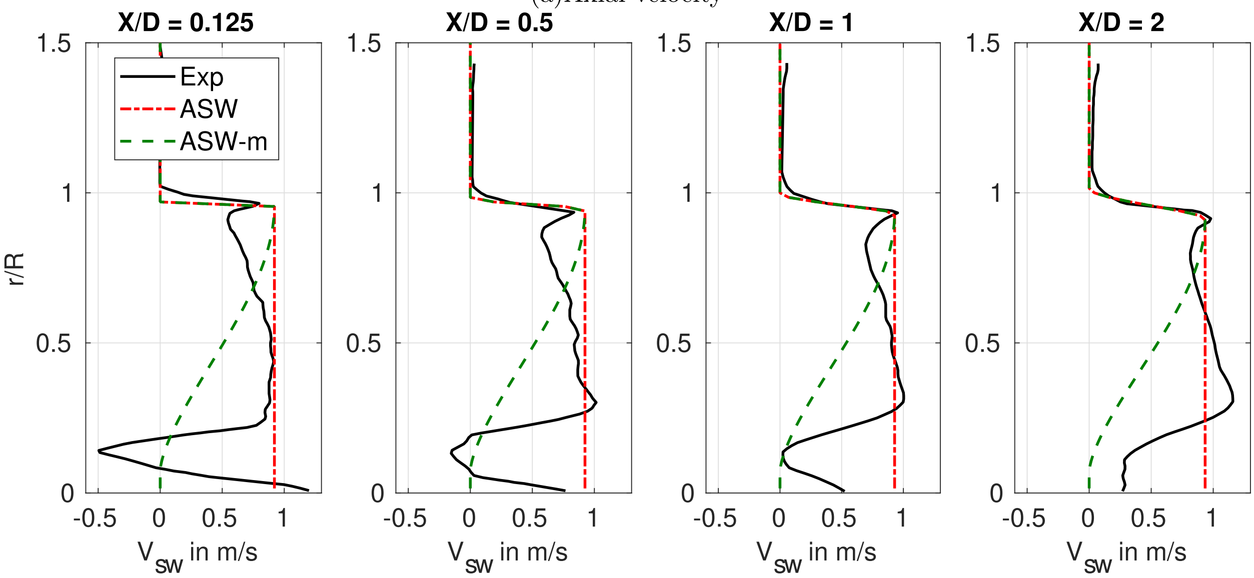

(b) Swirl velocity

Figure 19: CASE - D Advanced flow DA4002 (5000RPM), $\lambda = 0.64$, axial and swirl velocities evaluated at different streamwise location $\frac{x}{D}$ and different radial position $\frac{r}{R}$ (y-axis). Comparison of ASWING 5.96 and ASWING-m predictions with experimental data from Deters

References

[1] Albertson, M. L., Dai, Y. B., Jensen, R. A., and Rouse, H. (1950). Diffusion of Submerged Jets. *Transactions of the American Society of Civil Engineers*, 115(1):639–664.

[2] Betz, A. (1920). Zeitschr f Flugtechnik u Motorl.

[3] Deters, R. (2014). *Performance and slipstream characteristics of small-scale propellers at low Reynolds numbers*. PhD thesis, Graduate College of the University of Illinois.

[4] Deters, R. W., Ananda, G. K., and Selig, M. S. (2015). Slipstream Measurements of Small-Scale Propellers at Low Reynolds Numbers. In *33rd AIAA Applied Aerodynamics Conference*, Dallas, TX. American Institute of Aeronautics and Astronautics.

[5] Deters, R. W., Ananda Krishnan, G. K., and Selig, M. S. (2014a). Reynolds Number Effects on the Performance of Small-Scale Propellers. In *32nd AIAA Applied Aerodynamics Conference*, Atlanta, GA. American Institute of Aeronautics and Astronautics.

[6] Deters, R. W., Ananda Krishnan, G. K., and Selig, M. S. (2014b). Reynolds Number Effects on the Performance of Small-Scale Propellers. In *32nd AIAA Applied Aerodynamics Conference*, Atlanta, GA. American Institute of Aeronautics and Astronautics.

[7] Drela, M. (1999). Integrated simulation model for preliminary aerodynamic, structural, and control-law design of aircraft. In *40th Structures, Structural Dynamics, and Materials Conference and Exhibit*, St. Louis,MO,U.S.A. American Institute of Aeronautics and Astronautics.

[8] Drela, M. (2008). ASWING 5.81 Technical Description — Unsteady Extension. page 42.

[9] Drela, M. (2009). ASWING 5.86 Technical Description — Steady Formulation. page 57.

[10] Froude, W. (1889). Ibidem Vol 30 p 390 1889.

[11] Glauert, H. (1935). *AIRPLANE PROPELLERS*, volume IV of *Aerodynamic Theory*. New-York, springer edition.

[12] Goates, J. T. (2018). Development of an Improved Low-Order Model for Propeller-Wing Interactions.

[13] Hong, J.-H., Yeh, P.-H., and Chiew, Y.-M. (2020). Prediction of Mean Axial Velocity of a Free Turbulent Propeller Jet. *Journal of Hydraulic Engineering*, 146(3):04019070.

[14] Lam, W., Hamil, G., Song, Y., Robinson, D., and Raghunathan, S. (2011). A review of the equations used to predict the velocity distribution within a ship's propeller jet. *Ocean Engineering*, 38(1):1–10.

[15] Leng, Y., Bronz, M., Jardin, T., and Moschetta, J.-M. (2020). Slipstream Deformation of a Propeller-Wing Combination Applied for Convertible UAVs in Hover Condition. *Unmanned Systems*, 08(04):295–308. Publisher: World Scientific Publishing Co.

[16] Leng, Y., Yoo, H., Jardin, T., Bronz, M., and Moschetta, J.-M. (2019). Aerodynamic Modeling of Propeller Forces and Moments at High Angle of Incidence. In *AIAA Scitech 2019 Forum*, San Diego, California. American Institute of Aeronautics and Astronautics.

[17] Leng Yuchen (2020). *Aerodynamic design of long endurance convertible UAV*. PhD thesis, Université de Toulouse, ISAE-SUPAERO, Toulouse.

[18] Li Volsi, P., Gomez-Ariza, D., Gojon, R., Jardin, T., and Moschetta, J.-M. (2022). Aeroacoustic optimization of MAV rotors. *International Journal of Micro Air Vehicles*, 14:175682932110708.

[19] Phillips, W. F. (2004). *Mechanics of flight*. Wiley, New York.

[20] Prandtl, L. and Betz, A., editors (2009). *Ergebnisse der Aerodynamischen Versuchsanstalt zu Göttingen - IV. Lieferung*, volume 7 of *Göttinger Klassiker der Strömungmechanik*. Göttingen University Press, Göttingen.

[21] Rankine, W. (1865). Transactions Institute of Naval Architects. Technical Report 6.

[22] Ribner, H. S. (1945a). Propeller in Yaw. NACA Technical Report 820.

[23] Ribner, R. (1945b). Formulas for propellers in Yaw and chats of the side force derivative. Technical Report 819.

[24] Veldhuis, L. (1996). Analysis of propeller slipstream effects on a trailing wing.

[25] Veldhuis, L. L. M. (2004). Review of Propeller-Wing Aerodynamic Interference.

[26] Veldhuis, L. L. M. (2005). *Propeller wing aerodynamic interference*. s.n., S.l. OCLC: 840392156.

[27] Wei, M., Chiew, Y.-M., and Cheng, N.-S. (2020). Recent advances in understanding propeller jet flow and its impact on scour. *Physics of Fluids*, 32(10):101303.

Adresse postale
ISAE-SUPAERO
10 avenue É. Belin – BP 54032
31055 Toulouse CEDEX 4 – France

Téléphone
33 (0)5 61 33 80 80

Site internet
www.isae-supaero.fr